THESIS FOR THE DEGREE OF LICENTIATE OF ENGINEERING

Surfactant Adsorption on Pt Nanoparticles and its Impact on Catalysis

PUVANESWARI TELUCHINA-APPADU

Department of Physics

CHALMERS UNIVERSITY OF TECHNOLOGY

Gothenburg, Sweden 2026

Surfactant Adsorption on Pt Nanoparticles and its Impact on Catalysis
Puvaneswari Teluchina-Appadu

© PUVANESWARI TELUCHINA-APPADU, 2026.

Department of Physics
Chalmers University of Technology
SE-412 96 Gothenburg
Sweden
Telephone + 46 (0)31-772 1000

Cover:
Artistic rendition of micelles approaching and binding to a Pt nanoparticle with its unique set of surface defects and grains.

Printed by Chalmers Digitaltryck
Gothenburg, Sweden 2026

Surfactant Adsorption on Pt Nanoparticles and its Impact on Catalysis

PUVANESWARI TELUCHINA-APPADU
Department of Physics
Chalmers University of Technology

Abstract

The optical and catalytic properties of metallic nanoparticles depend on composition and surface functionalisation. In practical environments, nanoparticle surfaces are rarely pristine but instead frequently covered by organic molecular ligands originating from synthesis or deliberate functionalisation. An experimental challenge in colloidal synthesis is that any change in ligand identity or coverage is accompanied by subsequent variations in the nanoparticle size, morphology, or surface structure. Therefore, changes in catalytic activity measured with the different nanoparticles obtained cannot be solely attributed to the effects of the ligands.

This licentiate thesis investigates ligand–nanoparticle interactions through controlled and reversible adsorption–desorption cycles on lithographically fabricated Pt nanoparticles supported on a surface and with well-defined geometry. By employing initially ligand-free Pt nanoparticles, the influence of adsorbed molecular layers is examined without the shape variability typically encountered in colloidal systems. Cetyltrimethylammonium bromide (CTAB) is used as a model surfactant due to its well-characterized amphiphilic structure and concentration-dependent interfacial organization. A mild chemical reduction protocol enables repeated ligand removal while preserving nanoparticle integrity, allowing systematic comparison of multiple surface coverages on the same nanoparticle ensemble.

Nanoplasmonic sensing is utilized to monitor CTAB adsorption and re-arrangement in real time, exploiting the sensitivity of localized surface plasmon resonances to changes in the surrounding dielectric environment. Ensemble measurements constitute the primary experimental approach and reveal reproducible trends in adsorption kinetics and layer stability. The catalytic oxidation of ascorbic acid is employed as a model reaction to evaluate how ligand coverage influences reaction rate. A distinct impact of ligand coverage on catalytic activity is revealed. A preliminary single nanoparticle experiment is also presented, demonstrating the feasibility of resolving ligand adsorption at the level of individual nanoparticles. Together, the results show that ligand shells influence access to the nanoparticle surface and catalytic reaction rates, and that these effects can be investigated by using nanoplasmonic sensing protocols.

Keywords: CTAB, Pt nanoparticles, nanoplasmonic sensing, heterogeneous catalysis, ascorbic acid, ligand effects, single nanoparticle

“On sait qu’on ne sait pas, mais on veut savoir, alors on cherche.”
“We know that we do not know, but we want to know, so we search.”

\- *Étienne Klein*
(Translation mine)

List of Appended Papers

This thesis is based on the following appended papers:

Paper I: Teluchina-Appadu, P., Altenburger, B., Fritzsche, J. & Langhammer, C.
Bulk solution concentration dependent CTAB adsorption on Pt nanoparticles and its impact on the catalytic decomposition of ascorbic acid
In manuscript

My Contribution to Appended Papers

Paper I: I fabricated all samples using nanofabrication techniques and developed the complete experimental protocol, including the implementation of a nanoplasmonic sensing setup enabling *in situ* measurements of surfactant adsorption kinetics. I established a mild wet-chemical cleaning procedure for the removal of surfactants without altering the nanoparticle structures, thereby enabling subsequent adsorption studies at different bulk surfactant concentrations on the same sample. In addition, I developed the chemical protocol for catalytic reaction testing. I co-performed the catalytic measurements together with Björn Altenburger and carried out ToF-SIMS and XPS with Sushree Dash, and SEM characterization of the samples. I also prepared the first draft of the manuscript.

Other Publications Not Included in The Thesis

Paper I: Teluchina-Appadu, P., Daviddi, E., Kanoufi, F., Noël, J-M. & Lemineur, J-F.
Bubble Imaging of Galvanic Currents in Nanoscale Hydrazine−Oxygen Fuel Cells.
ACS Electrochem. ***2025**, 1,* 10, 2165–2176

Contents

1 Introduction

1.1 Nanoscience and Technology

The first mention of the concept of "nanotechnology" is attributed to Richard Feynman through a famous lecture held in 1959, titled 'There is plenty of room at the bottom'[1]. In his lecture, Feynman drew attention to the emergence of technologies that enable the controlled production and characterization of ultrasmall objects comprised of down to a few atoms or molecules. When at least one geometrical dimension of the ultrasmall object is less than 100 nm, nanostructures and nanoparticles are obtained. Their production and application underpin modern nanoscience and nanotechnology, which have become an integral part of many areas of technology with immense practical relevance[2], as shown in **Figure 1-1**.

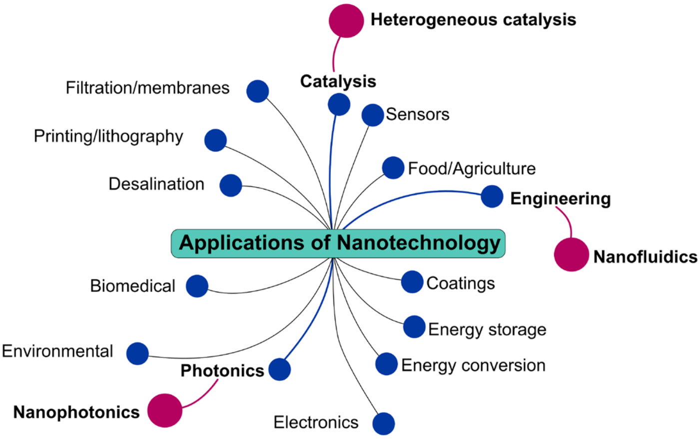

Figure 1-1. ***Conceptual map of the broad applications of nanotechnology.*** *The paths highlighted in purple mark the applications covered in this licentiate thesis and range from heterogeneous catalysis, via engineering to nanofluidics, and finally via photonics to nanophotonics*[2].

Different classes of nanomaterials are based either on how many of their three dimensions that are truly nanoscale and on their chemical composition[3]. According to these definitions, so-called nanoparticles and quantum dots encompass objects with all three dimensions at the nanoscale. Accordingly, nanotubes, nanowires and nanochannels are obtained when two dimensions are at the nanoscale and thin films and nanosheets are obtained when one dimension is at the nanoscale. Lastly, there can be systems that are not nanoscale in any dimension but that are built up of nanostructures, for instance nanoparticle dispersions or bundles of nanowires and zeolites. Nanomaterials in general can be purely carbon-based (graphene, fullerenes…), organic (polymers, micelles, liposomes...) and inorganic (metal, metal oxide, ceramic…) or composite structures[3]. The key reason that makes all of these systems interesting is that they exhibit optical, electronic, magnetic, chemical or structural properties that differ significantly from their bulk counterparts, and that often are size dependent and, thus, rationally tunable.

In my work, I am specifically interested in metallic nanoparticles because they possess tunable optical properties due to, so-called localized surface plasmon resonance (LSPR, **Chapter 2**) and interesting chemical properties that find wide application in heterogeneous catalysis (**Chapter 3**). There are two principal routes to make metal nanoparticles, namely top-down or bottom-up approaches. In the top-down approach, a bulk metal is transformed into nanoparticles, for instance, by ball milling or laser ablation[4]. In contrast, in bottom-up approaches, molecules, atoms or small particles self-assemble to form nanoparticles or nanostructures, such as in chemical vapor deposition used widely for lithography-based nanofabrication on surfaces, but also in sol-gel processes and colloidal synthesis, which enables the large scale production of metal nanoparticles[5]. In colloidal synthesis metal salt precursors dissolved in solution are chemically reduced to metal atoms using a reducing agent. As shown in **Figure 1-2**, above a critical concentration, $C_{\mathrm{min}}^{\mathrm{nuclei}}$, these metal atoms form a tiny stable seed particle, which subsequently further grows into a metal nanoparticle by attaching more metal atoms from the solution.

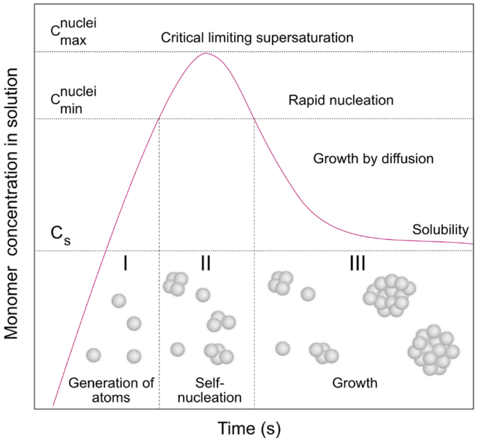

Figure 1-2. ***LaMer model of nucleation and growth.*** *In the first stage (I), metal precursors are reduced to metal atoms that accumulate in solution, leading to an increase in monomer concentration. In the second stage (II), when the concentration exceeds the critical supersaturation threshold for nucleation,* C_{min}^{nuclei} *, a short burst of nucleation occurs, resulting in the rapid formation of stable nuclei. These nucleation events consume monomers and cause a decrease in monomer concentration. In the third stage (III), once the concentration falls below* C_{min}^{nuclei}*, further nucleation is suppressed, while already formed particles continue to grow. Here, "growth by diffusion" refers to the diffusion-limited transport of monomer species from the bulk solution to the nanoparticle surface, where they are incorporated into the crystal lattice. At later stages, particle size evolution may also proceed through Ostwald ripening, in which smaller particles dissolve and redeposit onto larger ones. Growth continues until the monomer concentration approaches the equilibrium solubility concentration* C_S*, where no further net nucleation occurs and particle growth becomes negligible*[6].

To prevent the aggregation of these growing colloidal particles, so-called "ligands" are added to the colloidal suspension[7–9]. These ligands can be polymers, surfactants or ions that attach to the surface of the nanoparticles and thereby prevent two particles from getting too close (and thereby merging) either by steric hindrance effects and/or by electrostatic repulsion[7,10]. Furthermore, since such ligands often preferentially bind to specific surface facets of a growing colloidal nanoparticle and thereby slow down or completely block the attachment of new metal atoms to this specific facet, they can be used to control the shape of colloidal nanoparticles, as shown in **Figure 1-3**.

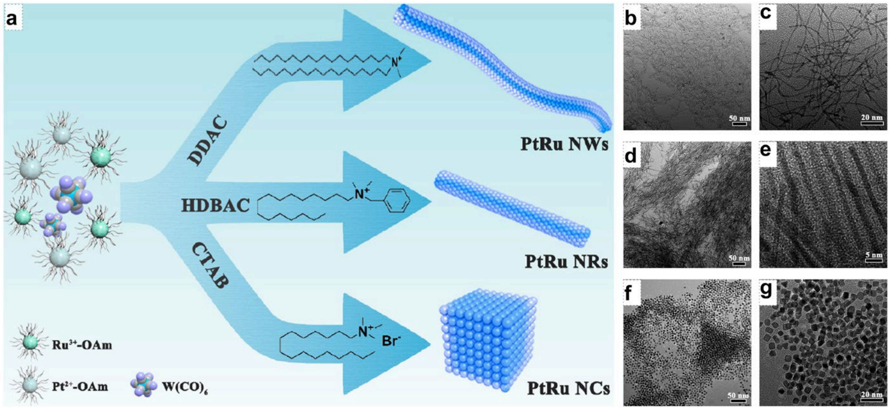

Figure 1-3. ***Impact of using different surfactants during colloidal synthesis.*** *a) Schematic illustration of different colloidal synthesis routes when using different surfactants, i.e., Dimethyldioctadecylammonium chloride (DDAC), hexadecyldimethylbenzyl ammonium chloride (HDBAC) or cetyltrimethylammonium bromide (CTAB), to form PtRu nanocrystals as an example for the general concept. Evidently, three different nanostructures with differing morphologies and facets are obtained, i.e., nanowires (NWs), nanorods (NRs) and nanocubes (NCs). Their representative TEM images are included on the right: b,c) for PtRu NWs, d,e) for PtRu NRs and f,g) for PtRu NCs. The nature of the surfactant is shown to be critical for the structure of the nanocrystals obtained. Adapted from Dong et al* [11].

1.2 Catalysis on Nanoparticles

Colloidal metal nanoparticles in general, and those with engineered shapes in particular, are of great interest in catalysis[12–15]. The term 'catalysis' was coined in 1836 by a Swedish chemist, Berzelius. Derived from Greek, it conveys the idea of 'breaking down' and 'loosening'. Specifically, in a catalytic process, reactants are "loosened" and "broken down" to form products. In heterogeneous catalysis, this happens on the surface of metal nanoparticles (the catalyst), which are not consumed themselves in the process but make the chemical reaction to occur faster by providing an alternative reaction route with a lower activation barrier[16]. A catalyst may also affect the selectivity of a reaction, meaning that it changes the preference of forming one product rather than another one by facilitating a distinct chemical route. Catalytic processes are ubiquitous in nature, as enzyme-mediated reactions in living organisms and also in photosynthesis in plants[17]. Catalysis has been used by humans for millennia, with early examples including fermentation and brewing documented from 6000-5800 BC and about 13,000 years ago respectively[18,19]. It remains central to many large-scale industrial processes today. The production of sulfuric acid, one of the most widely used industrial chemicals, key for fertilizer production and chemical synthesis, requires the oxidation of sulfur dioxide to sulfur trioxide using vanadium (V) oxide as catalyst during the, so-called, contact process[20,21]. Similarly, developed at the onset of the First World War, the Haber-Bosch process enables the large scale ammonia synthesis using iron-based catalysts promoted by metal oxides for the reaction of nitrogen to hydrogen, and is fundamental to fertilizer production[22]. Fritz Haber was awarded the Nobel Prize in chemistry in 1918 for developing this process. The importance of catalysis is further underscored by multiple Nobel prizes awarded in this field, for instance for asymmetric organocatalysis[23] in 2021 and for chemical processes on solid surfaces[24] in 2007. More broadly, catalytic processes are critical in oil refining, where Pt and Co-Mo or Ni-Mo based catalysts are widely used, and in organic synthesis where metals such as Pt, Pd, Ni, Rh and Ru facilitate dehydrogenation, hydrogenation, oxidation, isomerization and cyclisation reactions[25].

Focusing on the role of noble/transition metal nanoparticles in catalysis specifically when they are less than 10 nm, a first key trait is the high surface area to volume ratio. This on one hand ensures efficient use of the often scarce and costly raw materials since the reaction only occurs on the atoms localized at the surface and on the other hand, provides abundant reaction sites for adsorption and activation of reactants and intermediates[26]. One example is the use of transition metal catalysts are Pt, Pd and Rh nanoparticles used in the three-way catalytic converters to oxidize lethal carbon monoxide and hydrocarbons into less harmful carbon dioxide and to reduce nitrogen oxides into nitrogen[27]. A second example is PdAu nanoparticles that are used for the large-scale production of vinyl acetate monomer, a precursor to make polyvinyl acetate, a polymer used in paints, adhesives and textile finishes[28].

1.3 Optical Properties of Nanoparticles

A second key trait of metal nanoparticles, which is important for my thesis, is the fact that they interact strongly with visible light via LSPR excitations, i.e. coherent collective oscillations of the free electrons in the particles[29,30]. This leads to strong light scattering and absorption at the resonance frequency of this electron oscillation, which in turn, makes single metal nanoparticles visible in a dark-field optical microscope and enables optical sensing and spectroscopy experiments from single particles[31,32]. The frequency at which LSPR occurs depends on the size, shape, composition and surroundings of the nanoparticles. Therefore, any change in LSPR frequency can be backtracked to changes in any of these parameters. This, in turn, makes the LSPR an optical probe naturally "built into" metal nanoparticles that enables the tracking of changes to the nanoparticles themselves, or their local environment, in a wide range of scenarios that include biosensing[33–35], gas sensing[36–40] or the study of catalysts and catalytic reactions[41].

1.4 Ligands in Nanoparticle Catalysis

The relative difference of the effects are often difficult to disentangle due to the fact that if the type of ligand or the ligand concentration is changed for a colloidal synthesis process, while keeping the metal precursor and reducing agent unchanged, entirely different nanoparticles will be obtained (**Figure 1-3**), which therefore most likely also exhibit entirely different catalytic properties. In other words, it is very difficult to judge whether any observed change in catalytic properties is due to a difference in ligand type, coverage, or surface arrangement, or due to the different morphology of the nanoparticle, or a combination of the two.

Numerous experimental studies have examined how surface ligands influence the catalytic behaviour of metal nanoparticles[42,43]. A recurring limitation in this literature is that modifications of ligand identity or ligand coverage are frequently accompanied by simultaneous and insufficiently controlled changes in nanoparticle structure, including variations in particle diameter, particle size distribution, morphology, surface facet distribution, defect density, and oxidation state. Since each of these parameters *independently* affects catalytic activity and selectivity, isolating intrinsic ligand effects remains challenging. Consequently, reported trends often reflect a combination of structural and chemical contributions rather than ligand–surface interactions alone.

The interplay between ligand coverage and catalytic activity was evident in early investigations of alkanethiolate-capped Pd nanoparticles applied to allyl alcohol isomerization, where reduced ligand coverage was correlated with increased turnover frequencies[44]. The enhanced activity was initially attributed to reduced site blocking and improved accessibility of Pd surface atoms. However, subsequent work demonstrated that varying ligand concentration during synthesis also altered the particle size distribution and surface structure, producing particles with differing proportions of low-coordination surface atoms[45]. Because such structural variations are known to influence catalytic rates independently, the experimentally observed decrease in activity at higher ligand coverage could not be attributed solely to ligand blocking. Although the catalytic trend was reproducible, the mechanistic origin therefore remained ambiguous.

To reduce this ambiguity, later studies implemented post-synthetic ligand exchange protocols in which nanoparticles were first synthesized under fixed nucleation and growth conditions to obtain comparable particle diameters and surface site distributions, followed by controlled ligand exchange[46]. These approaches were applied in alkene and alkyne hydrogenation reactions, where decreasing thiolate coverage consistently increased hydrogenation rates and, in some cases, shifted selectivity toward fully hydrogenated products[47]. Despite improved structural control, ligand coverage was typically quantified ex situ, and the dynamic state of the ligand shell under reaction conditions was not directly monitored. Partial ligand desorption, conformational rearrangement, or oxidative degradation during catalysis was therefore not excluded, limiting the certainty with which coverage-dependent activity trends could be interpreted.

Beyond thiolate systems, ligand functionality was shown to influence catalytic performance in a reaction-specific manner. Investigations of Pd nanoparticles functionalized with nitrogen-containing ligands in selective hydrogenation reactions, reported that increased ligand coverage reduced overall conversion while certain amine-terminated ligands enhanced selectivity toward partially hydrogenated products[48]. These studies also reported improved catalyst stability, here referring to retention of catalytic activity over repeated reaction cycles in addition to resistance to aggregation. However, the meaning of *stability* varies between studies. In some cases, it refers to retention of catalytic activity over repeated cycles, whereas in others it denotes structural integrity, resistance to poisoning, or preservation of ligand coverage. This complicates direct comparison between reports.

In related investigations of alkyne hydrogenation to alkenes, ligand-capped Pt and $CoPt_3$ nanoparticles altered product selectivity by modulating competitive adsorption between ligand molecules and reactant intermediates on the surface[49]. Density functional theory calculations reproduced qualitative selectivity trends by comparing adsorption energetics, yet the computational models relied on static ligand shells and idealized surface geometries that did not incorporate surface restructuring or solvent interactions observed experimentally. Agreement between experiment and theory was therefore achieved at a qualitative level, while quantitative predictive capability remained limited.

Ligand effects have also been reported in electrocatalytic systems. Imidazolium-functionalized Ag nanocrystals demonstrated enhanced electrochemical CO_2 reduction to CO, exhibiting higher faradaic efficiencies and reduced onset potentials compared to unmodified particles[50]. These improvements were attributed to both electronic interactions at the metal surface and modification of the local interfacial environment, including altered hydrophobicity and stabilization of reaction intermediates. Because electronic and microenvironmental effects occurred concurrently, their individual contributions to catalytic performance were not independently quantified.

Computational investigations further examined ligand–nanoparticle interactions in the context of selective hydrogenation and oxidation reactions, identifying trends in charge redistribution and adsorption energetics associated with electron-donating and electron-withdrawing ligands[51–53]. While these studies provided mechanistic insight, they frequently employed simplified solvent models, small clusters and limited configurational sampling of ligand arrangements. Their quantitative transferability to experimentally relevant catalytic systems was therefore constrained.

Collectively, these studies demonstrate that ligands influence nanocatalysis through intertwined electronic, steric, and microenvironmental mechanisms that affect catalytic activity, selectivity, and apparent stability. At the same time, they highlight a persistent methodological limitation: the difficulty of isolating intrinsic ligand effects from concurrent variations in particle morphology, surface structure, and ligand shell configuration under operating conditions[54]. As a result, it often remains unclear to what extent observed catalytic trends arise from genuine ligand–surface interactions as opposed to artefacts introduced by experimental design or uncontrolled structural changes. This ambiguity underscores both the fundamental and technological importance of further investigation and motivates the development of experimental approaches that maintain a constant nanoparticle structure while enabling controlled and independently quantifiable modification of ligand coverage. Such strategies are essential for unambiguously identifying and quantifying ligand effects and, ultimately, for the rational tailoring of ligands to optimize specific catalytic reactions.

As a final part of this introduction, I discuss the motivation for extending catalytic activity studies to the single-nanoparticle level, where ligand adsorption and catalytic activity can be investigated on individual nanoparticles. The main motivation for such experiments is that, at the atomic level, each nanoparticle is unique, with its own combination of size, shape, defects, faceting, and composition, including contaminants or intentional alloying elements. It is therefore reasonable to expect that each nanoparticle may display a distinct pattern of surfactant adsorption and a distinct reactivity for a given reaction[55–57]. Consequently, even in an ensemble of nominally identical nanoparticles (i.e., produced with the level of control state-of-the-art nanofabrication and colloidal synthesis methods can provide), the individuals may have sizably different properties which are not resolved due to ensemble averaging in traditional experiments[58]. Hence, to see beyond this ensemble average, experiments with single nanoparticle resolution are necessary[59–61].

To this end, a significant number of methods that enable the investigation of catalysis on single nanoparticles in situ or in operando exist today[62]. For example, liquid-cell Transmission Electron Microscopy (TEM) allows the monitoring of a single nanoparticle's grain structural dynamics during a reaction in the liquid phase[63], while differentially pumped in situ TEM[64,65] or similar concepts of fluidic cells[63,66–68] also enable in situ studies of catalyst particles during catalytic reactions in the gas phase. However, as key limitations, TEM only provides information about the state of the nanoparticle, but not about the products formed and the high energy electron beam always comes with the risk of beam-induced artefacts[63,69–71]. Similar limitations apply to Quick Scan X-ray Absorption Fine Structure (QXAFS) analysis[72]. Another interesting method is Scanning ElectroChemical Cell Microscopy (SECCM)[73], where an electrolyte-filled capillary with several micrometers opening is approached to a conducting substrate decorated with catalytic nanoparticles. The droplet at the tip forms a closed system defined by the glass surface and the meniscus of the liquid droplet, which remains attached to the capillary. If the wetting area is small enough to cover only a single nanoparticle, the activity of that one nanoparticle in this closed system is studied. The fact that the substrate is conductive and a thin metal wire can be inserted into the capillary allows the establishment of a 2-electrode electrochemical cell on a single nanoparticle. The limitations are, however, that the current measured is very small, that only electrochemical reactions can be studied, that mass transport limitations rapidly dominate and that the reactants' concentration change over time with solvent evaporation.

Important contributions in single nanoparticle catalytic studies have also been achieved by using single-molecule fluorescence microscopy[74]. This technique can resolve catalytic turnovers with single-event precision, thereby overcoming ensemble averaging and revealing the true heterogeneity of nanoscale catalysts. By immobilising metal nanoparticles and quantifying individual fluorescent reaction events, operando kinetic measurements have been performed under ambient conditions with millisecond resolution, allowing reaction pathways, adsorption equilibria and turnover frequencies to be extracted directly[74,75]. Another defining insight from single-particle studies is that nanoparticles synthesized under nominally identical conditions nevertheless display a broad distribution of intrinsic properties. For example, product dissociation rates cluster into distinct subpopulations for Au nanoparticles studied[55,56]. These heterogeneities are invisible in ensemble assays, which average different kinetics into deceptively simple kinetics. As another example, single-molecule studies of Pt nanoparticles in an oxidative N-deacetylation reaction and a reductive N-deoxygenation reaction showed that spontaneous surface restructuring can change the availability of active sites over time, leading to different catalytic behaviour even within the same nanoparticle[57]. To extend single particle catalysis studies beyond reactions that involve fluorescent species, a competitive imaging strategy (COMPEITS) has been introduced[76]. In this approach, a non-fluorescent target reaction is indirectly visualised by competing it with a fluorescent reporter reaction. Local suppression of reporter turnover signals the presence and the rate of the non-fluorescent pathway. By using this strategy, it was possible to achieve nanometer-scale spatial mapping of heterogeneous reactivity and facet-dependent kinetics on individual photocatalysts under operando conditions.

In addition to single-molecule fluorescence microscopy approaches, catalytic reactions at the single nanoparticle level can also be investigated by using advanced vibrational spectroscopies, such as Tip-enhanced Raman Spectroscopy (TERS) and Shell-Isolated Nanoparticle-Enhanced Raman Spectroscopy (SHINERS). TERS combines a plasmonically active scanning probe with Raman spectroscopy, providing nanometer-scale chemical resolution. It has been used to monitor catalytic transformations directly on individual nanostructures, revealing sub-particle spatial heterogeneity in product formation[77]. Subsequent developments, including the introduction of chemically robust zirconia-protected probes, have facilitated TERS measurements under liquid-phase and near-operando conditions, demonstrating nanoscale mapping of catalytic processes in realistic environments[78,79]. Complementary to TERS, ultrathin-shelled plasmonic nanoparticles have been used as non-invasive Raman enhancers and pioneered SHINERS[80]. This approach enables strong surface-enhanced Raman signals to be obtained from otherwise non-SERS-active catalytic surfaces, such as single crystal electrodes and metal oxides, without perturbing their chemistry. More recently, SHINERS has been integrated into operando multi-sensor platforms for monitoring both temperature and surface species on single catalyst particles during reaction[81]. Collectively, TERS and SHINERS provide nanoscale chemical identification and mechanistic insights that complement the turnover-resolved reactivity obtained using single-molecule fluorescence microscopy.

Finally, prior work has demonstrated that nanoplasmonic sensing using nanofabricated nanoparticle arrays provides a powerful ensemble-level platform to investigate both ligand adsorption and surface reactions in situ. For example, the localized surface plasmon resonance (LSPR) response of nanofabricated arrays of Pd nanoparticles was monitored to study the impact of surfactants and stabilizers on hydrogen sorption kinetics in these Pd nanoparticles[82]. The work showed that ligands can significantly modify hydrogen uptake and release dynamics, illustrating that nanoplasmonic arrays enable real-time monitoring of ligand-induced changes in surface reactions at the ensemble level.

Along similar lines, early plasmonic sensing studies systematically employed alkanethiol self-assembled monolayers with varying carbon chain lengths to probe the, so-called, thin-film sensitivity and electromagnetic field decay length of plasmonic nanostructures. For instance, it was demonstrated that controlled thiol adsorption on gold nanorings enabled quantitative determination of the near-field decay length of the localized surface plasmon resonance[83]. These studies collectively established that LSPR is well suited for monitoring ligand adsorption in situ and, separately, for probing surface reactions and interfacial phenomena. However, these two aspects have rarely been combined within a single experimental platform, that is, using LSPR *both* to monitor ligand binding and subsequently to quantify catalytic activity on the same nanostructures. Bridging this gap constitutes a central motivation of the present work.

Building on these ensemble nanoplasmonic sensing approaches, our group has developed nanofluidics-based methodologies that enable the extension of investigations outlined above at the nanoparticle ensemble level, to the single-nanoparticle level. In particular, nanofluidic platforms have been established for studying single-particle catalysis both in the gas-phase[84–88] and in the liquid phase[59–61,89,90]. In essence, by analysing light scattered either from the catalyst nanoparticle itself or from the nanofluidic channel hosting the particle, approaches termed Nanofluidic Scattering Microscopy (NSM) and Nanofluidic Scattering Spectroscopy (NSS) enable the tracking of dynamic structural and compositional changes of individual catalyst particles in real time, while simultaneously quantifying their catalytic activity.

1.5 Aim of Thesis

The aim of this thesis is to develop an experimental framework for investigating how ligand adsorption on metal nanoparticles affects surface accessibility and heterogeneous catalysis. To this end, the work primarily establishes a systematic nanoplasmonic sensing approach at the ensemble level, in which repeated ligand adsorption, removal, and catalytic measurements can be performed on the same lithographically fabricated nanoparticle arrays while maintaining a constant nanoparticle structure. This enables direct correlation of ligand-induced surface modifications with catalytic response. As a first step toward extending such studies beyond ensemble averaging, the thesis also includes a preliminary single-nanoparticle experiment that demonstrates the feasibility of resolving ligand adsorption on an individual nanoparticle localized inside a nanofluidic channel.

2 Optical Properties of Metal Nanoparticles

Despite nanoparticles being “invisible”, they interact strongly with light in the visible spectral range due to a phenomenon called Localised Surface Plasmon Resonance (LSPR). LSPR induces strong scattering and absorption of light at a given resonance wavelength, which is defined by the particle’s dimensions and geometry, as well as its surroundings, and which produces very vibrant colours. To access these beautiful colours, people have mixed solutions of gold ions with a reducing agent and obtained bright ruby red solutions of gold nanoparticles for around 1500 years already[29]. Stained-glass makers used the same method to produce beautiful, stained-glass objects with different colours. One such creation is a relic called the Lycurgus cup and others are part of church windows all over the world (**Figure 2-1**).

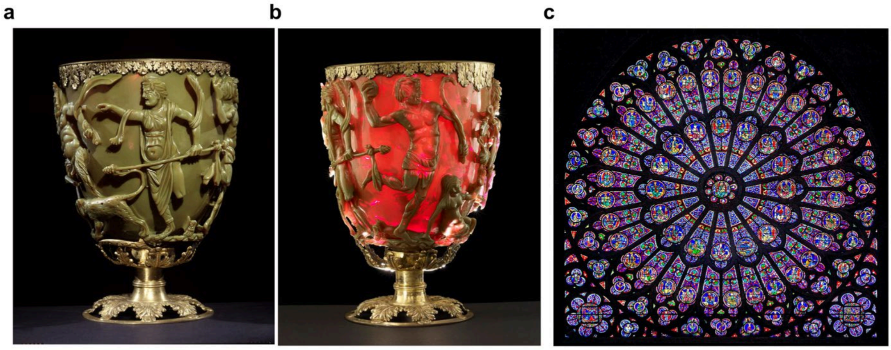

Figure 2-1: ***Colouration arising from localised surface plasmon resonance (LSPR) in metal nanoparticle-containing glass.*** *The Lycurgus Cup, a 4th-century Roman artefact containing Au and Ag nanoparticles, appears green under external illumination, where scattering dominates a), and red under internal illumination, where absorption dominates b). c) Rose window of the Notre-Dame de Paris Cathedral, composed of stained glass containing noble-metal nanoparticles responsible for the vivid colours. Images reproduced under Creative Commons licenses: a,b) © The Trustees of the British Museum, CC BY-NC-SA 4.0; c) J. A. Workman, CC BY-SA 3.0.*

When metal nanoparticles are exposed to the time-dependent electromagnetic field of light, the free electrons in the metal move within this field relative to the stationary atomic nuclei, resulting in a time-dependent charge separation. Therefore, a restorative force acts to reposition the electrons and this combination of electrons moving away from the nuclei and the restorative force pulling them back, in similarity with a harmonic oscillator. In other words, in a simple approximation, the system can be defined by characteristics, such as spring constant and damping, which are influenced by the nanoparticle's shape, size and composition[91]. Furthermore, like any oscillator, the system has an eigen- or resonance frequency where a small energy input leads to a strong oscillation. Hence, when the nanoparticles resonate at a specific frequency of light, the corresponding very strong collective oscillation of the free electrons gives rise to a very strong interaction with light. When decaying, the coherent collective electron oscillation dephases and either re-emits a photon ("scattering") or absorbs it ("absorption") via hot-electron excitations that eventually thermalize with the phonon bath[92]. At the same time, the polarization of the electronic system during LSPR excitation creates locally enhanced electromagnetic fields extending tens of nanometers from the nanoparticles. Inside this, so-called, "sensing volume", tiny changes in the polarizability of the medium occupying this volume can be detected, as they lead to a change in the LSPR frequency[93,94]. This mechanism forms the foundation for so-called LSPR sensing in various applications, including biosensing, chemical sensing and gas sensing[35,95–97]. Apart from the immediate surroundings of the nanoparticle, the frequency at which the resonance occurs is also specific to various other factors, such as size, shape and composition of the nanoparticles, as evidenced in **Figure 2-2d**. Each nanoparticle type has its own specific sensitivity to changes in its surroundings, where sharp geometric features and Drude-like metals like Ag and Au typically maximize this effect[94].

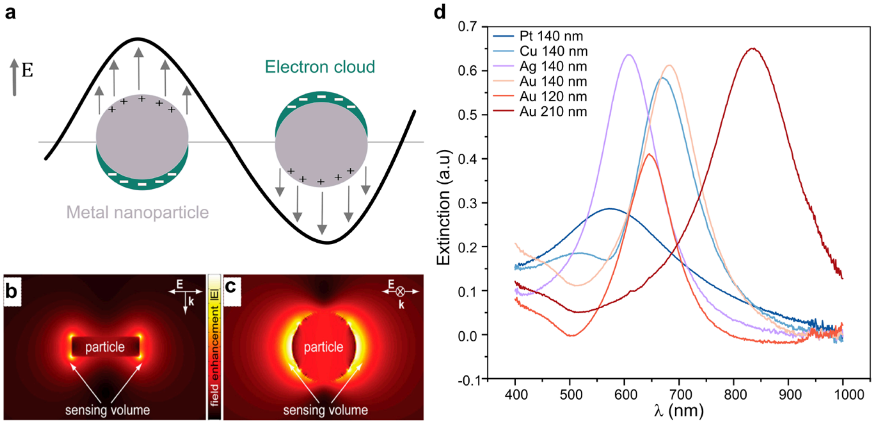

Figure 2-2. LSPR and electric field enhancement effect around a nanoparticle. *a) Interaction of light with a nanoparticle, causing the excitation of resonant collective oscillations of the free electron system, also known as Localised Surface Plasmon Resonance, LSPR. b) Side view and c) top view of an 80 nm diameter and 20 nm height Au disk illuminated at the LSPR resonance wavelength. The colour scale illustrates the electric field strength enhancement effect around the nanoparticle, as obtained from finite-difference-time domain*[98] *simulations. It constitutes a spatially confined volume – the sensing volume – around the nanoparticle, extending tens of nanometres away from the surface, inside which tiny polarizability changes can be detected, such as the adsorption of a layer of molecules or the change of the refractive index of the medium. d) The distinct LSPR peaks obtained in a UV-visible extinction spectrum for different quasi-random nanodisk arrays made by Hole-mask Colloidal Lithography*[99] *on a glass substrate. The examples here are arrays of nanodisks consisting of Pt with 140 nm diameter, Cu with 140 nm diameter, Ag with 140 nm dimeter, Au with 140 nm diameter, Au with 120 nm diameter and Au 210 nm in diameter. All nanodisks are 30 nm thick. b) and c) are adopted from Langhammer et al*[95].

To describe analytically the LSPR phenomenon, one can consider a simplified model of a metallic sphere, with a radius, *r*, significantly smaller than the wavelength of light. Gustav Mie's analytical solutions can be used in this model to obtain the electromagnetic response of the sphere[100,101]. In its simplest form, the quasi-static approximation is applied, which means that the particle is so small that the electric field is assumed not to vary spatially across the sphere at any given time.

When exposed to a uniform electric field, $\vec{E}_0$, a dipole moment is induced in the metallic sphere and can be expressed by:

$$\vec{P} = \alpha \vec{\mathrm{E}}_0, \tag{2.1}$$

where α represents the sphere's polarizability. The polarizability is calculated by the following expression:

$$\alpha = 4\pi \mathrm{r}^3 \frac{\varepsilon_\mathrm{m} - \varepsilon_\mathrm{d}}{\varepsilon_\mathrm{m} + 2\,\varepsilon_\mathrm{d}} \tag{2.2}$$

where r is the sphere's radius, and ε_m is the metal's complex dielectric function. ε_d represents the dielectric function of the surrounding medium of the sphere. Since ε_d for dielectrics, such as glass, varies very little with wavelength in the visible range it is often assumed to be constant[102]. Resonance occurs at the frequency where the polarizability is maximal, i.e., when the denominator is zero. For a given ε_d of the medium, the maximum polarizability condition is satisfied only for a given ε_m, whose value is wavelength dependent. Thus, at that specific wavelength, the resonance peak occurs.

The strength of the interaction between the nanoparticle and light can be quantified by an optical cross-section, C_i, whether it be for absorption, scattering or extinction[29]. The corresponding absorption, scattering and extinction cross sections can be written as

$$C_{\text{extinction}} = k\text{Im}(\alpha) \quad (2.3)$$

$$C_{\text{scattering}} = \frac{k^4}{6\pi}|\alpha|^2 = \frac{8\pi}{3}k^4r^6\left|\frac{\varepsilon_m - \varepsilon_d}{\varepsilon_m + 2\,\varepsilon_d}\right|^2 \quad (2.4)$$

$$C_{\text{absorption}} = C_{\text{extinction}} - C_{\text{scattering}} \quad (2.5)$$

The wavenumber associated with the incoming light is denoted by $k = \frac{2\pi}{\lambda}$, with λ as the wavelength in the surrounding medium. From the above expressions, it is again clear that maximum polarizability leads to a maximum in absorption and scattering. Another interesting aspect is the fact that absorption is proportional to r^3, while scattering is proportional to r^6, resulting in absorption dominating in small particles, while scattering dominates in larger particles. Therefore, for very small nanoparticles, where scattering is considered negligible, it can be approximated that $C_{\text{absorption}} \simeq C_{\text{extinction}} \simeq k\text{Im}(\alpha)$.

The complex dielectric function of the metal, $\varepsilon_m(\omega)$, is frequency- and thus also wavelength-dependent to a greater extent than is ε_d[103].

As mentioned earlier, there is a condition at which resonance occurs, where the denominator in **equation 4.2** equals zero, meaning that the real part of the denominator vanishes and losses are not too large. This condition is written explicitly as:

$$Re[\varepsilon_m(\omega)] = -2\,\varepsilon_d \quad (2.6)$$

and it provides the wavelength at which LSPR occurs for a given dielectric function of the surrounding medium.

Different metals have different $\varepsilon_m(\omega)$. To analytically describe the dielectric function, the Drude model is a simplified approach that works well for free electron metals, such as Ag and Au[29]:

$$\varepsilon_\mathrm{m}(\omega) = 1 - \frac{\omega_\mathrm{p}^2}{\omega^2 + i\Gamma\omega}, \tag{2.7}$$

ω_p denotes the bulk plasma frequency, and Γ denotes the damping factor, which accounts for energy dissipation either through radiative (scattering) processes or non-radiative processes, such as interband or intraband transitions in the metal. The plasma frequency is given by:

$$\omega_\mathrm{p} = \sqrt{\frac{Ne^2}{\epsilon_0 m_e}} \tag{2.8}$$

where N, e, m_e and ϵ_0 represent the density of free electrons, the fundamental charge of an electron, its mass and the permittivity of vacuum, respectively. By substituting **equation 4.6** into **equation 4.7**, and by assuming minimum damping, which means Γ is null, the LSPR frequency of a Drude sphere can, thus, finally be expressed as:

$$\omega_\mathrm{LSPR} = \frac{\omega_\mathrm{p}}{\sqrt{1 + 2\,\varepsilon_\mathrm{d}}} \tag{2.9}$$

or, in wavelength as:

$$\lambda_\mathrm{LSPR} = \lambda_\mathrm{p}\sqrt{2\,\varepsilon_\mathrm{d} + 1} \tag{2.10}$$

where λ_p denotes the bulk plasma wavelength, given by $\lambda_\mathrm{p} = \frac{c}{\omega_\mathrm{p}}$, where c is the speed of light.

2.1 LSPR Sensing

From **equation 2.10**, it becomes clear that any change in the dielectric function of the surrounding medium, ε_d, will yield a change in the LSPR wavelength. It also becomes clear that any change to ω_p or λ_p of the metal nanoparticle also will induce a change in the LSPR wavelength, λ_{LSPR}. Such a change of the bulk plasma frequency is equivalent to a change of the nanoparticle itself in terms of its chemical state. The absorption of hydrogen into Pd nanoparticles, where hydrogen occupies interstitial lattice sites is one example of such a process[104]. In the Drude metal framework, hydrogen occupation of interstitial sites both expands the Pd lattice and contributes electronic charge to the Pd host, thereby modifying the electron density, N. As a consequence, ω_p changes (see **equation 2.8**), thus also ω_LSPR (see **equation 2.9**), and eventually λ_LSPR. This is the fundamental principle of what has become to be known as "plasmonic hydrogen sensing"[105].

To give an example for more "traditional" nanoplasmonic sensing[105], i.e., a scenario where a change in ε_d leads to a change in λ_{LSPR}, I used a chip containing a quasi-random array of Au nanodisks with 140 nm diameter and 30 nm height (**Figure 2-3**) as a nanosensor. As can be seen, the surface of the chip is densely populated with an average density of eleven nanodisks per μm^2.

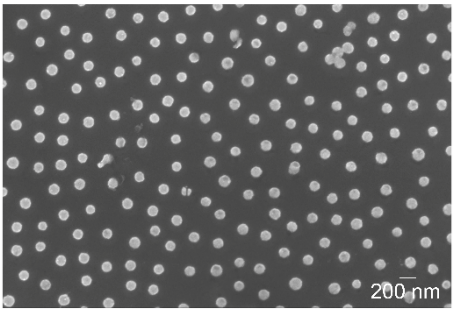

Figure 2-3. ***Scanning Electron Microscopy (SEM) image of magnification ×20000 of a representative plasmonic sensing chip.*** *A quasi-random array of Au nanodisks with 140 nm diameter and 30 nm height nanofabricated on a silicon substrate using Hole-Mask Colloidal Lithography. A few aggregations of the nanodisks can also be noticed and are the consequence of the electrostatic self-assembly process used to create that nanolithography mask, as described in detail in* ***Chapter 4****.*

To illustrate the plasmonic sensing principle, I have exposed a similar chip as depicted in **Figure 2-3** (with the difference that the substrate was transparent fused silica) to an ethylene glycol-water mixture at systematically varied concentrations to systematically alter ϵ_d, and measured the spectral shift of λ_{LSPR}, which I term $\Delta\lambda_{LSPR}$ (**Figure 2-4a**). From such a measurement, by extracting $\Delta\lambda_{LSPR}$ for each ethylene glycol concentration, a calibration curve can be established, along with the, so-called, bulk refractive index sensitivity (BRIS) of the plasmonic sensor defined as $s = \frac{d\lambda_{LSPR}}{dn}$, where the refractive index of the medium is defined as $n = \sqrt{\varepsilon_d}$ (**Figure 2-4b).** For the specific plasmonic sensing chip that I have used for this example experiment, I obtained a BRIS of 161.4 nm/RI unit. It is important to note that the BRIS obtained is for the given nanoparticle-analyte-solvent system only, and that this value changes for other types of nanoparticles, analytes or in other solvents[106,107].

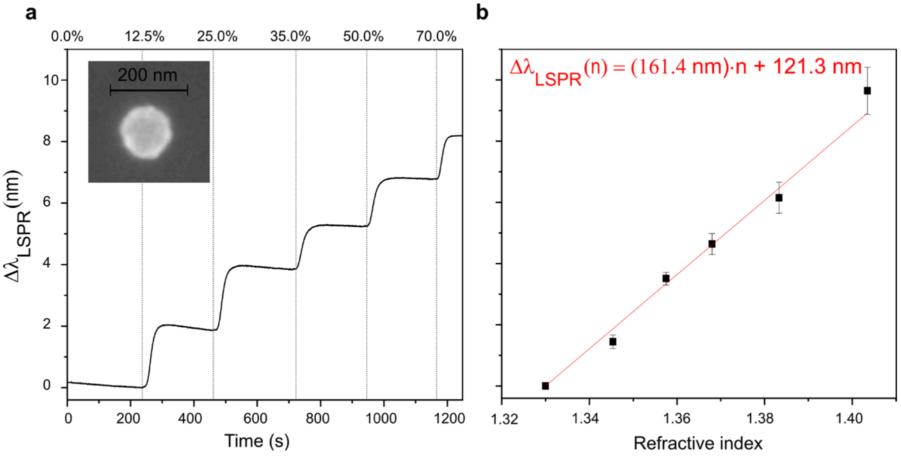

Figure 2-4. ***Proof of principle of plasmonic refractive-index sensing.*** *I used a quasi-random array of Au nanodisks with 140 nm in diameter and 30 nm height, fabricated onto a fused silica substrate using Hole-Mask Colloidal Lithography. Extinction spectra were recorded in real time while the sample was sequentially exposed to aqueous ethylene glycol solutions of increasing concentration (0.0%-70.0% w/v). a) Temporal evolution of the plasmonic centroid shift relative to its equilibrium value in water,* $\Delta\lambda_{LSPR}$. *Vertical dashed lines indicate the arrival of each new solution at the chip's surface. Increasing ethylene glycol concentration results in a monotonic red-shift of* $\Delta\lambda_{LSPR}$ *due to the higher refractive index, n, of the surrounding medium.* $\Delta\lambda_{LSPR}$ *after approximately 60 s, indicating that the new equilibrium concentration is reached in the measurement chamber. The inset shows an SEM image of Au nanodisk in the used array. b) Calibration curve obtained from three independent measurements using chips from the same nanofabrication batch. Mean equilibrium* $\Delta\lambda_{LSPR}$ *values are plotted as a function of bulk refractive index*[108]*, and the sensor sensitivity is extracted from the slope of the linear fit. Error bars represent the standard deviation of three measurements.*

In this thesis, I have used nanoplasmonic sensing to monitor ligand adsorption on metal nanoparticles, relying mostly on the induced change to ε_d by the binding of the ligand molecules and the subsequent formation of a thin layer on the nanoparticle surface as the sensing mechanism. However, since charge transfer between ligand molecules and the metal likely also takes place in many cases, a small contribution from a change in ω_p is also to be expected[83].

3 Surfactant-Nanoparticle Systems

3.1 Surfaces of Metals and Metal Nanoparticles

Understanding ligand adsorption on metallic nanoparticles requires consideration of the structural and electronic characteristics of nanoparticle surfaces. At the nanoscale, surfaces and interfaces dominate material behaviour, and metallic nanoparticles are particularly governed by interfacial structure. A metallic nanoparticle with a diameter of a few tens of nanometers contains a substantial fraction of its atoms at or near the surface rather than in the bulk. At the surface, there are terraces, step edges, kinks, and adatoms. Such structural motifs arise from the termination of the crystal lattice and from deviations in local atomic coordination. A commonly used conceptual framework for describing crystalline surfaces is the Terrace–Ledge–Kink (TLK) model[109], illustrated in **Figure 3-1a**. This model highlights that even a single crystallographic facet contains atomic-scale structural variation. In nanoparticle systems, additional diversity arises from differences in size, shape, crystallographic facets, grains, defects, and impurities, even between particles prepared under nominally identical conditions (**Figure 3-1b**). As a consequence, no two nanoparticles are strictly identical, and surface-mediated processes measured on an nanoparticle ensemble, such as ligand adsorption, inherently represent an *average* over many distinct interfacial configurations. For studies that probe collective surface phenomena, such as the adsorption and restructuring of molecular layers, this structural variability does not necessarily manifest as individually resolvable events but rather as broadened or averaged responses. The interface should therefore be regarded not only as the site of interaction between a nanoparticle and its environment, but also as the origin of particle-to-particle variability that influences how ensemble measurements conducted on a large number of nanoparticles are to be interpreted.

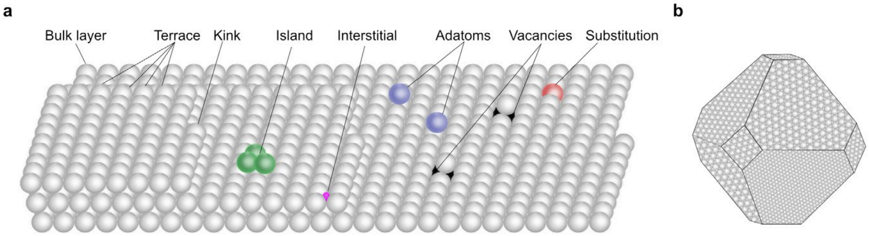

Figure 3-1. ***Atomic surface heterogeneity on crystalline surfaces and nanoparticles.*** *a) Terrace–ledge–kink (TLK) model illustrating the variety of atomic sites present on a crystalline surface at the nanoscale. b) Schematic nanoparticle illustrating the coexistence of multiple crystallographic facets, edges, corner sites and packing densities, extending the TLK description to nanoscale geometries.*

In practice, nanoparticle surfaces are rarely pristine. Molecules originating from synthesis, storage, or deliberate functionalization frequently adsorb onto the surface and form molecular layers whose organization depends on parameters, such as concentration, temperature, and solvent conditions[110].
Ligand shells on metal nanoparticles span a broad chemical range. Common ligand classes include surfactants, amphiphilic molecules composed of a hydrophilic headgroup and a hydrophobic tail, such as cetyltrimethylammonium bromide (CTAB) or sodium dodecyl sulfate (SDS), polymers including poly(vinylpyrrolidone) (PVP), polyethylene glycol (PEG), and polymethyl methacrylate (PMMA), as well as small molecular ligands, such as thiols, amines, citrate, or catechol derivatives. These species differ in size, flexibility, and binding strength, leading to variations in layer thickness, surface coverage, and reversibility of adsorption[111,112].

The organization of ligand shells at nanoparticle interfaces is governed by a balance of intermolecular and surface forces, including van der Waals interactions, electrostatic attraction or repulsion, and the hydrophobic effect[113–115]. In aqueous environments, the hydrophobic effect constitutes a dominant driving force for amphiphilic molecules to minimize exposure of non-polar segments to water, thereby promoting both self-assembly in solution and adsorption at solid interfaces. Counterion binding and ionic strength further influence this equilibrium by screening electrostatic interactions and altering the effective headgroup charge[115].

Essentially, ligands serve two functions. During colloidal synthesis, they can selectively bind to crystallographic facets, thereby influencing nanoparticle shape evolution[112,116,117]. They stabilize nanoparticles against aggregation through steric and electrostatic repulsion[113,117]. In addition, ligands may be introduced intentionally to tailor interfacial properties, for example by tuning hydrophilicity, introducing steric or electrostatic filtering, or biasing the local chemical environment toward preferential interaction with specific molecular species[10,109]. Thus, the presence of ligands is therefore both unavoidable and, in many cases, desirable.

In this work, the surfactants are used as ligands. They remain present at a nanocatalyst surface under realistic operating conditions if they are not explicitly removed[116,117]. Understanding how such molecular layers influence catalytic accessibility is therefore essential for interpreting catalytic performance. Surfactants are commonly categorized according to the charge of their headgroup as cationic, anionic, zwitterionic, or non-ionic. Each class exhibits distinct adsorption behaviour, interaction strength with metal surfaces, and sensitivity to environmental parameters, such as ionic strength and temperature[115,118]. Tail length, branching, and headgroup chemistry further determine packing density and effective layer thickness[118]. These structural variables ultimately define how surfactant shells modify the accessibility and physicochemical environment of nanoparticle surfaces and, consequently, how surface-mediated processes, such as catalytic reactions, can proceed[110,117].

3.2 Surfactants in Solution

Surfactant molecules exist as isolated entities in solution at low concentrations. However, above a characteristic concentration known as the critical micelle concentration (CMC), they spontaneously aggregate into micelles, while at even higher concentrations they may form additional ordered structures[115]. This behaviour arises from the hydrophobic effect, which drives the non-polar tails to minimize contact with water while exposing the polar headgroups to the surrounding solvent. As a consequence, above the CMC, the concentration of free surfactant monomers often differs significantly from the total surfactant concentration present in the system. Furthermore, parameters such as temperature, salt concentration, and molecular geometry strongly influence this aggregation behaviour. Concepts including the aggregation number — defined as the average number of surfactant molecules forming an aggregate — the Krafft temperature, corresponding to the minimum temperature at which sufficient monomer solubility enables micelle formation, and the cloud point, describing temperature-induced phase separation in certain surfactant systems, characterize transitions between soluble, micellar, and phase-separated states[115]. These factors are particularly relevant when investigating surfactant adsorption onto solid interfaces, as adsorption kinetics depend on the dynamic equilibrium between free surfactant monomers and self-assembled aggregates present in solution. Micelles act as reservoirs that exchange monomers with the surrounding solution, while cooperative adsorption or restructuring of larger assemblies at the interface may also contribute depending on surface chemistry and solution conditions[115,118]. Consequently, in a solution above the CMC, the concentration of surfactant species available for adsorption onto a surface is governed by monomer–aggregate equilibria rather than total surfactant concentration alone[114].

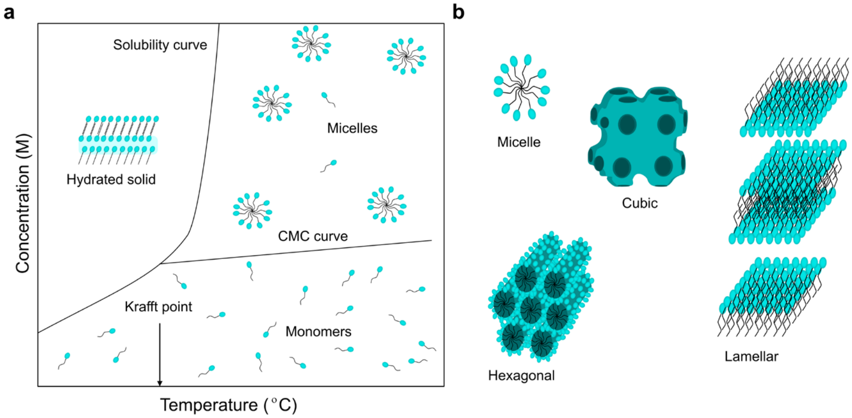

Figure 3-2. ***Temperature-dependent solubility and aggregation behaviour of ionic surfactants in aqueous solution.*** *a) Schematic temperature–concentration phase diagram illustrating the relationship between surfactant solubility and self-assembly. The Krafft point corresponds to the intersection between the surfactant solubility limit and the critical micelle concentration (CMC). Below the Krafft point, micelle formation is prevented because the equilibrium monomer solubility remains lower than the CMC, and excess surfactant persists as hydrated crystalline solid at elevated concentrations. Above the Krafft temperature, increased solubility allows the monomer concentration to exceed the CMC, enabling micelle formation. b) Representative aggregate morphologies formed with increasing concentration above the Krafft temperature, including spherical micelles and liquid-crystalline mesophases such as cubic, hexagonal, and lamellar structures*[115].

Temperature and concentration jointly govern the aggregation behaviour of ionic surfactants in aqueous solution through the Krafft phenomenon (**Figure 3-2a**). At low surfactant concentrations and temperatures below the Krafft temperature, surfactants exist exclusively as dissolved monomers. In this regime, the equilibrium solubility of surfactant monomers in water is lower than the CMC. As a result, the monomer concentration cannot reach the level required for micelle formation. Additional surfactant therefore precipitates as hydrated crystals rather than forming aggregates, preventing micellization under equilibrium conditions.

Upon increasing the temperature above the Krafft point, surfactant solubility increases sharply and the dissolved monomer concentration can reach and exceed the CMC, enabling spontaneous micelle formation. The CMC itself exhibits only a weak temperature dependence and often increases slightly with temperature, commonly attributed to reduced hydration of ionic headgroups and enhanced molecular mobility[115]. For CTAB, which has been studied exclusively in this thesis, the range is between 0.82 mM to 1.13 mM with a temperature range of 10 °C to 40 °C[119]. In general, the CMC of CTAB at room temperature is considered to be ≈ 1 mM. The Krafft point of CTAB has been reported to be between 20 °C to 25 °C[120]. Consequently, both temperature and concentration determine the population of molecular species present in solution and must be considered simultaneously when interpreting adsorption and interfacial processes.

At concentrations above the CMC, cooperative packing of amphiphilic molecules leads to progressively more ordered aggregate structures (**Figure 3-2b**). Spherical micelles dominate at moderate concentrations, while further increases in concentration promote the formation of liquid-crystalline mesophases, including hexagonal, cubic, and lamellar assemblies. The preferred aggregate geometry can be rationalized using the critical packing parameter (CPP),

$$CPP = \frac{v}{a_0 l} \tag{3.1}$$

where v is the hydrophobic tail volume, a_0 the effective headgroup area, and l the chain length[113]. The CPP provides a qualitative predictor of aggregate curvature, where v is the hydrophobic tail volume, a_0 the effective headgroup area, and l the chain length. Increasing CPP favours aggregates with reduced interfacial curvature. Approximate regimes include spherical micelles ($CPP < 1/3$), cylindrical or hexagonal assemblies ($1/3 < CPP < 1/2$), bicontinuous or cubic phases ($\sim 1/2$), and planar bilayers or lamellar phases ($CPP \approx 1$). In practice, these transitions occur gradually over concentration ranges and depend sensitively on ionic strength, counterion binding, and solvent composition[115]. With these different aggregates, the aggregation number also varies. For CTAB, the aggregation number is reported to be 95 for spherical micelles up to around 100 CMC, and increases for lower-curvature morphologies[120].

3.3 Surfactants on Solid Surfaces

Having considered surfactant behaviour in solution, we now turn to their interaction with solid surfaces. We first note that surfactant adsorption depends on both the chemical nature of the surface and the surfactant structure[121]. Importantly, surfactant adsorption kinetics are typically governed by the concentration of dissolved monomers rather than the total surfactant concentration, since micelles primarily act as dynamic reservoirs that buffer the monomer population through rapid exchange processes.

Nevertheless, lateral interactions between adsorbed surfactant molecules can induce cooperative adsorption, enabling the formation and restructuring of surface-bound aggregates, such as hemimicelles or bilayer-like layers depending on surface charge and solution composition. In addition, adsorption strength can vary across different crystallographic surfaces in general, and thus facets of a nanoparticle in particular, as variations in atomic coordination and surface electronic structure lead to site-dependent binding affinities[122].

Focusing on (when clean) hydrophilic or charged metallic surfaces, they may induce bilayer structures, patchy adsorption, or competitive binding with counterions[115,121]. The resulting surface assemblies can range from loosely packed bilayers to densely organized multilayers (**Figure 3-3a, c, e**). In contrast to high-energy oxide or metallic surfaces, hydrophobic surfaces, such as hydrocarbon-based polymer coatings, self-assembled alkyl monolayers, or graphitic carbon interfaces[113,118], typically promote tail-down monolayer formation, where favourable interactions between the non-polar surfactant chains and the surface drive adsorption (**Figure 3-3b, d, f**)[115,118,121].

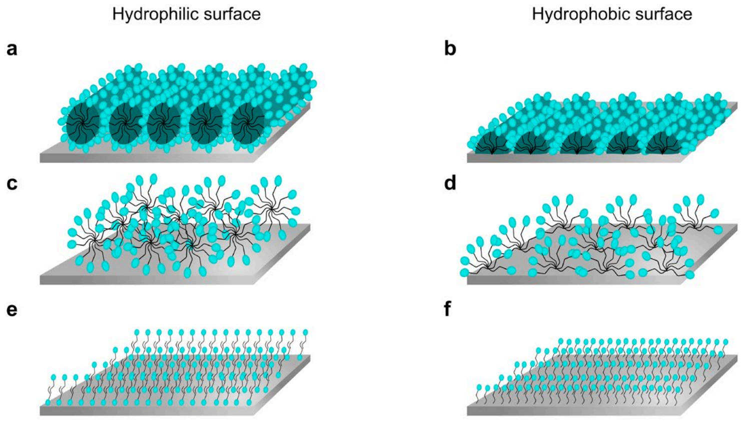

Figure 3-3. ***Schematic illustration of representative surfactant aggregates formed at solid–liquid interfaces in aqueous environments.*** *a, c, e) Structures typically observed on hydrophilic surfaces, such as clean metals, showing cylindrical aggregates, spherical micelles, and bilayer formations, respectively. b, d, f) Corresponding structures on hydrophobic surfaces, such as organic, polymeric coatings or graphitic carbon, illustrating hemicylindrical aggregates, hemispherical micelles, and monolayer coverage. Hydrophilic headgroups are depicted as blue spheres, whereas hydrophobic tail groups are represented by black chains. The schematics are qualitative and intended to convey general interfacial organization rather than exact molecular geometry*[121].

3.4 Surfactants in Nanocatalysis

Catalytic reactions occurring on nanoparticle surfaces proceed through a sequence of elementary steps, typically involving adsorption of reactants, surface diffusion and reaction, and desorption of products. In the absence of a catalyst, the transformation from reactants to products can often be represented by a comparatively high activation barrier E_1, as illustrated by the grey curve in **Figure 3-4**.

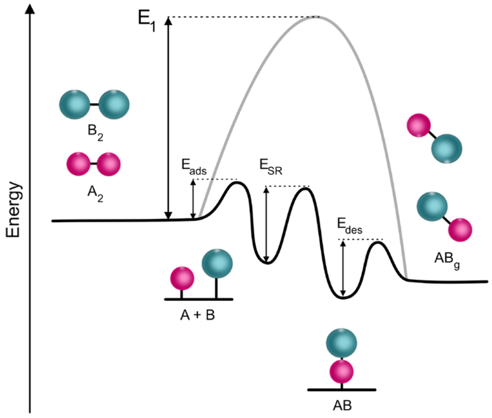

Figure 3-4. ***Schematic reaction energy diagram illustrating the difference between an uncatalyzed pathway (grey curve) and a nanoparticle-catalysed pathway (black curve).*** *The uncatalyzed reaction proceeds over a single activation barrier* E_1*, whereas the catalyzed pathway in its simplified representation is divided into multiple elementary steps corresponding to adsorption* (E_{ads})*, surface reaction* (E_{SR})*, and desorption* (E_{des})*. Although the catalyst lowers the individual activation barriers and thereby accelerates reaction kinetics, the overall free-energy difference between reactants and products remains unchanged.*

A catalyst instead provides an alternative reaction pathway consisting of multiple elementary steps, each associated with lower activation energies. While the catalyst accelerates the reaction kinetics, the overall thermodynamic driving force remains unchanged, as reflected by the equal energy difference between reactants and products in both pathways. For heterogeneous catalysis, the catalyzed pathway in its simples form typically consists of adsorption of reactants onto the nanoparticle surface, a surface reaction step via transition-state formation, and subsequent desorption of products. These stages are associated with distinct energetic barriers, denoted here as E_{ads}, E_{SR}, and E_{des}, respectively, as shown by the black curve in

Figure 3-4. The magnitude of these barriers is determined by the interaction strength between the surface and the reacting species[109].

According to the Sabatier principle, optimal catalytic performance is achieved at an intermediate interaction strength between the surface and the reactants: interactions that are too weak lead to insufficient adsorption and low surface coverage, whereas interactions that are too strong can result in site blocking or surface poisoning due to hindered desorption[109]. This is where it is critical to consider what happens if ligands in general, and surfactants in particular, are already adsorbed on the catalyst surface since their presence may, modify each elementary step by altering both steric accessibility of the active site(s) and the local electronic environment at the interface via charge transfer between ligand and surface. Accordingly, ligands can shift energies E_{ads}, E_{SR} and E_{des} by introducing local hydrophobic or electrostatic environments that selectively attract or repel certain reactants[109,123]. At the same time, ligands reduce the number of accessible adsorption sites and can impose diffusion barriers for molecules approaching the surface[124].

Beyond overall activity, ligands have also been reported to influence selectivity, defined as the preferential formation of one product over competing reaction pathways. For example, steric hindrance can exclude larger molecules or constrain adsorption geometries and electrostatic interactions can favor specific charge states and local polarity can bias the interfacial partitioning of reactants[50,51,125]. Through these mechanisms, ligand shells can act as interfacial “filters” that regulate which species reach the surface and which reaction routes are energetically favored. This introduces an inherent trade-off between activity and selectivity: conditions that maximize reaction rate may reduce selectivity, while conditions that enhance selectivity may decrease overall throughput[109]. Understanding this balance is therefore central to interpreting experimental observations of ligand adsorption, restructuring, and removal cycles on ligand-covered nanoparticle catalysts. Furthermore, if these effects are properly understood, they may enable new strategies for the rational design of catalyst materials in which the interplay between nanoparticle surfaces and ligand environments becomes a key design parameter.

3.5 Surfactants and the Optical Properties of Metal Nanoparticles

Ligand shells, such as those formed by surfactant molecules, influence not only the catalytic activity but also the optical response of metallic nanoparticles. LSPR is highly sensitive to the dielectric environment surrounding the nanoparticle, as well as to charge-transfer interactions at the metal surface[35,93,94]. Because the localized electromagnetic near-field decays exponentially away from the nanoparticle surface, LSPR shifts primarily report changes occurring within a scale of tens of nanometer adjacent to the interface[93,95,126]. Consequently, molecular adsorption occurring within this near-field region alters the effective local refractive index and electronic coupling at the metal interface, producing measurable changes in LSPR peak position, linewidth, and extinction[35,94]. These optical signatures provide a direct and label-free means of monitoring ligand adsorption and desorption processes in real time. Importantly, the reversibility or irreversibility of adsorption determines whether spectral changes are transient or persistent. Repeated adsorption–rinsing cycles combined with time-resolved tracking of LSPR peak position, extinction amplitude, and linewidth therefore provide insight into binding strength, layer stability, and potential interfacial restructuring[83,127].

To demonstrate these effects experimentally, **Figure 3-5** presents representative LSPR spectra and time-resolved peak shifts obtained in this work during a CTAB adsorption–rinsing cycle on Pt nanoparticle arrays**.** Upon exposure to 0.7 mM CTAB, the LSPR peak exhibits a clear red shift relative to the initial water condition, consistent with an increase in the effective local refractive index surrounding the nanoparticle due to surfactant adsorption. Simultaneously, a reduction in extinction amplitude and a narrowing of the peak linewidth are also observed. Time-resolved LSPR peak position tracking (**Figure 3-5c**) reveals a rapid adsorption following CTAB introduction, whereas subsequent rinsing with water results in only partial recovery toward the initial baseline. The persistence of the LSPR peak shift indicates that a fraction of CTAB molecules remains bound to the nanoparticle surface also after rinsing. Taken together, these observations demonstrate that LSPR spectroscopy provides a sensitive optical probe of ligand adsorption and interfacial molecular binding and restructuring during fluid-exchange conditions.

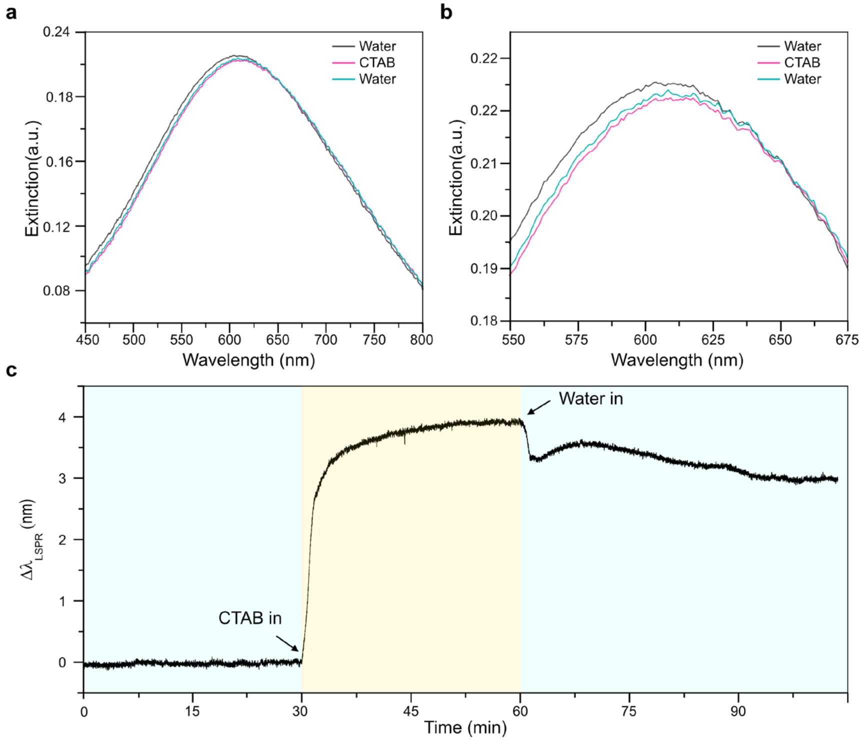

Figure 3-5. ***LSPR spectral response during a representative CTAB adsorption–water rinsing cycle.*** *a) Extinction spectra recorded in water, during exposure to a 0.7 mM CTAB solution for 30 min, and after rinsing with water for 30 min. CTAB exposure induces a red shift of the LSPR peak,* $\Delta\lambda_{LSPR}$*, accompanied by changes in linewidth and extinction amplitude relative to the initial water spectrum. b) Magnified view of the LSPR peak region highlighting subtle spectral differences between the three states. Following rinsing, the LSPR peak partially recovers but remains shifted relative to the initial water condition, indicating residual surface modification. c) Time evolution of* $\Delta\lambda_{LSPR}$ *during the cycle. Introduction of CTAB solution at 30 min induces a rapid red shift, while subsequent rinsing with water results in only partial recovery toward the initial baseline.*

4 Metal Nanoparticle Fabrication onto a Surface

At a very general level, there are two widely used methods to obtain ligand-free metallic nanoparticles on a substrate, namely photolithography and electron beam lithography (EBL)[128]. The photoresist used to make a mask in photolithography is sensitive to photons and the resolution of the structures obtained is in its simplest form defined by the diffraction limit of light and therefore only structures above a few hundred nanometres can be obtained. More advanced versions with much higher resolution exist but require advanced infrastructure[129]. Photolithography is a highly parallel process that enables the patterning of large surface areas efficiently. In the second case, EBL, the resist used is sensitive to electrons, and the spatial resolution is very high, i.e., a few nanometres. However, the time for exposing the sample increases considerably when a large surface is to be covered by nanoparticles. The reason is that EBL is a serial technique, where each individual nanostructure is exposed in sequence.

To strike a compromise between the two concepts presented above, so-called self-assembly based nanofabrication methods have been developed, where colloidal lithography in its many different versions is the most well-known one[130]. The core principle of colloidal lithography is to use the (most often electrostatic) self-assembly of colloidal nanoparticles on a surface to either form a quasi-random array of colloidal nanoparticles directly or to use the formed sparse monolayer of colloidal nanoparticles to create a nanolithography mask. This has the conceptual advantage that the self-assembly can cover large surface areas rapidly, while at the same time small nanostructures can be made as colloidal nanoparticles are available in the range from few to hundreds of nanometres.

The specific variant of colloidal lithography that I have used in this thesis to make my samples, Hole-Mask Colloidal Lithography (HCL)[99], is a method established nineteen years ago at Chalmers. This method exploits electrostatic self-assembly of polystyrene beads for patterning a polymer resist, where the diameter of the polystyrene beads defines the diameter of the holes in the resist mask used to transfer the pattern onto the substrate **(Figures 4-1 and 4-2)**.

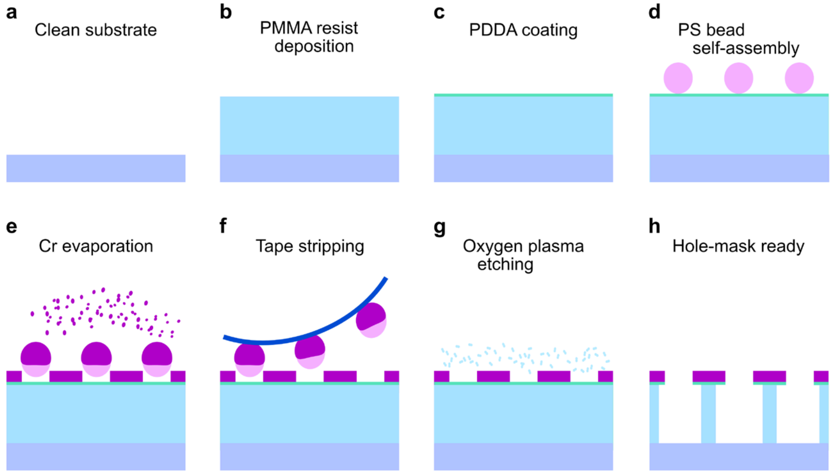

Figure 4-1. ***Hole-mask preparation steps in chronological order****. a) substrate cleaning/preparation by subsequent rinsing in acetone and isopropanol. b) PMMA sacrificial resist layer spin-coating. c) Positively charged PDDA polyelectrolyte coating application. (d Electrostatic self-assembly of PS nanobeads. e) Chromium mask evaporation. f) Tape stripping of PS nanobeads to create holes in the chromium mask to transfer the pattern into the resist. g) Oxygen plasma etching of the PMMA layer through the Chromium hole-mask. h) The final developed mask.*

The HCL nanofabrication method[99] requires the following subsequent steps **(Figure 4-1)**:

a) Substrate cleaning: A fused silica substrate (in my case 9 mm x 9 mm x 0.5 mm is cleaned by subsequent sonication in acetone and isopropanol (IPA) for 2 minutes each. The substrate is then blow-dried with a stream of N_2 gas. Acetone and isopropanol ensure the removal of organic contaminants and residual particles, respectively.

b) PMMA resist deposition: A solution of Polymethyl methacrylate (PMMA 4) of 0.2 wt.%, Mw = 950 000, from Microlithography Chemicals Corp. is drop-cast on the substrate. Subsequently, the chuck onto which the substrate is attached is spun at 2000 rpm for 60 seconds yielding a PMMA resist layer of ca. 280 nm thickness. The coated substrate is then soft baked at 170 °C for 3 minutes, to evaporate all solvent. After baking, the PMMA resist layer is gently ashed in oxygen plasma (50 W, 250 mTorr, 10 sccm) to increase the hydrophilicity of the surface, as required by the next step.

c) Poly (diallyl dimethylammonium chloride) coating: PDDA with MW = 100 000 – 200 000, a positively charged polymer, is drop-cast from a 0.2 wt.% aqueous solution and incubated for 1 minute. Subsequently, the substrate is rinsed with Milli-Q water and blow dried using N_2 gas, forming a PDDA monolayer on the surface that renders the surface positively charged.

d) PS bead self-assembly: A 0.2 wt.% 140 nm in diameter PS bead aqueous solution is drop-cast onto the substrate, incubated for 2 minutes and then rinsed for 20 seconds in milli-Q water, followed by blow drying by N_2. Due to the electrostatic attraction between the negatively charged PS beads to the positively charged PDDA layer, the beads adhere to the substrate. At the same time, due to the electrostatic repulsion between the charged beads, the latter will become randomly dispersed into a quasi-random sparse monolayer.

e) Cr mask evaporation: A 15 nm thick Cr layer is electron-beam evaporated onto the sample to form the mask by leaving circular openings at the position of the PS beads.
f) PS bead tape stripping: A tape is placed flat on the surface of the substrate covered with PS beads and Cr mask layer. Subsequently stripping the tape removes the PS beads which are glued to the tape, leaving behind circular holes in the Cr layer which have the same dimension as the PS beads' diameter.
g) Oxygen plasma etching: The sample is exposed to 5 minutes of O_2 plasma treatment (50 W, 250 mTorr, 10 sccm) to transfer the hole-pattern into the PMMA resist, down to the silica substrate. Here, etching time determines the amount of undercut of the PMMA resist under the Cr layer. A certain amount of undercut is necessary to enable mask lift of eventually.
h) Hole-mask ready: A sparse quasi-random array of holes, whose diameter is defined by the PS beads, is now present and the mask is now ready.

The steps described above are generic for any kind of sample prepared by HCL. The subsequent steps described below and schematised in **Figure 4-2** are specific for the samples I have worked with in this thesis, which were quasi-random arrays of Pt (as well in a more limited fashion Au and Pd) nanodisks with 140 nm diameter. To fabricate them, I e-beam evaporated first a 2 nm thick Cr adhesion layer into the hole-mask **(Figure 4-2a)**. Subsequently, I e-beam evaporated 25 nm of the metal of choice to grow the nanodisks in the hole-mask **(Figure 4-2b)**. As the final step, the hole-mask is lifted-off by immersing the sample into acetone that dissolves the PMMA layer **(Figure 4-2c)**. The metal nanodisk array is then left behind on the silica surface.

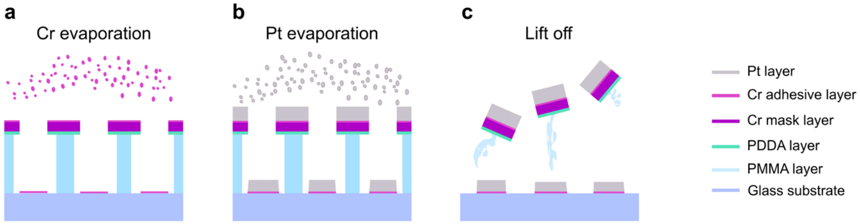

Figure 4-2. Fabrication of the metal nanoparticles I used in my thesis using a Hole-Mask prepared as depicted in Figure 4-1. *a) E-beam evaporation of a 2 nm thick Cr adhesion layer. b) E-beam evaporation of the metal of choice (here Pt) to grow the nanodisks. c) Lift-off to remove the mask, leaving only the sparse quasi-random array of nanodisks on the substrate, c.f.* ***Figure 4-3****).*

A wide range of nanoparticle sizes and compositions can be obtained with HCL fabrication. To illustrate that versatility, I showcase a range of samples I have made during my project **(Figure 4-3a)**. The different colours obtained for the samples arise from the LSPR which depends on nanodisk diameter and metal used. An SEM image of a representative sample surface, i.e., a quasi-random array of 140 nm Pt nanodisks is shown in **Figure 4-3b**. This constitutes the sample type I have used for the surfactant adsorption, as well as catalysis experiments. Finally, it is also worthy of noting that HCL is not limited to a single element nanoparticles, but can also be used to make arrays of alloy nanoparticles by subsequently evaporating multiple metal layers through the hole-mask that are transformed into an alloy by annealing at elevated temperatures to enable solid state diffusion[36,131,132].

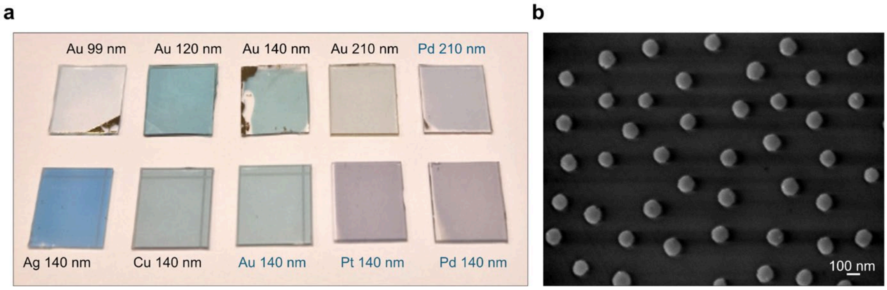

Figure 4-3. ***HCL fabricated samples.*** *a) Selection of samples that I have nanofabricated using HCL onto fused silica substrates. All disks are 30 nm (black labels) or 25 nm thick (blue labels). The different colours are the consequence of LSPR excitations with a dependence on their size and material. b) Top-view SEM image at ×45000 magnification of a sample nanofabricated on a silica surface and comprised of a quasi-random array of Pt nanodisks with 140 nm diameter.*

5 CTAB Adsorption on Pt Nanoparticle Arrays and its Impact on Catalysis

As discussed in **Chapter 3**, colloidal nanoparticles are commonly capped with ligands to prevent aggregation in solution and to direct particle shape during synthesis, and these ligands can form a variety of structures both in solution and at solid–liquid interfaces. Because such ligands remain at the nanoparticle surface when the particles are transferred to an application, unless specific ligand-removal procedures are applied, it is important to understand how they adsorb, reorganize, and persist at the surface, and how they affect performance. In heterogeneous catalysis, ligands have been reported to block or modify catalytically active surface sites and can thereby influence reaction rates and selectivity.

While the long-term goal of this work is to investigate ligand effects at the level of individual catalyst nanoparticles using single-particle plasmonic sensing and nanofluidics, this thesis first establishes an ensemble-level experimental protocol to study ligand–nanoparticle interactions in a controlled and systematic way. The experimental concept is illustrated in **Figure 5-1**. Instead of using colloidal nanoparticles in solution, catalyst nanoparticles are fabricated onto an inert surface by nanolithography, which eliminates the need for stabilizing ligands during particle preparation. This makes it possible to first characterize a catalytic reaction on clean, ligand-free nanoparticles to establish a baseline, then expose the same nanoparticles to a selected ligand system and evaluate the catalytic reaction again under otherwise identical conditions. Afterward, the ligands can be removed by a tailored cleaning procedure to recover the baseline state and verify that the intrinsic catalytic activity of the nanoparticles has not changed during the experimental cycle. In principle, this sequence can then be repeated on the same nanoparticle ensemble using either a different ligand system or the same ligand at a different concentration. This latter possibility is particularly relevant for surfactants, which are known to form different interfacial structures depending on concentration and may therefore influence catalysis differently under different adsorption conditions.

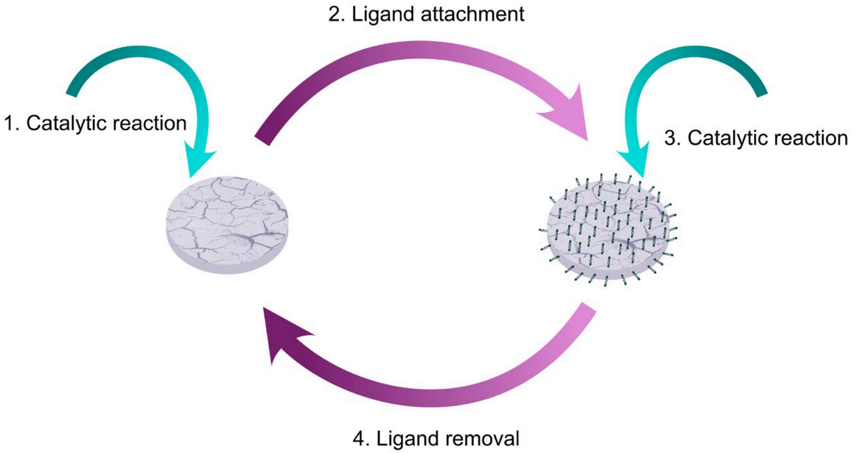

Figure 5-1. ***The experimental concept developed in this thesis to assess the impact of ligands on catalytic reactions on a nanoparticle surface.*** *A catalytic reaction is characterized on a clean ligand-free nanoparticle nanofabricated onto an inert surface. Ligands are then attached to the nanoparticle's surface forming a ligand-covered nanoparticle by a simple adsorption step. The same catalytic reaction is then characterized on the now ligand-covered nanoparticle. Subsequently, the ligands can be removed again using a tailored cleaning procedure to re-establish the clean ligand-free nanoparticle on which the catalytic reaction can be characterized one more time to account for any change imposed on the nanoparticle's intrinsic reactivity by the experimental procedure. If desired, after this first circle, another type of ligand or the same type of ligand at different concentration can be adsorbed on the nanoparticle, and the catalytic activity evaluation cycle repeated. Hence, in principle, this cycle of attaching and removing ligands, while characterizing the catalytic activity, can be repeated many times on the same nanoparticle(s), given the particle(s) is (are) not changing by this procedure.*

Because ligand surface arrangement depends strongly on ligand concentration in solution, it is important to characterize ligand adsorption before assessing catalytic activity. In this chapter, I use the localized surface plasmon resonance (LSPR) response of plasmonic Pt nanoparticle arrays as an intrinsic probe of CTAB adsorption and removal in situ. Specifically, Pt nanoparticle arrays fabricated on fused silica by Hole-Mask Colloidal Lithography are used as a model catalyst platform, CTAB is used as the model surfactant, and the catalytic decomposition of ascorbic acid is used as the model reaction. The sensing workflow used to monitor ligand adsorption and removal is illustrated in **Figure 5-2**. Together with catalytic activity measurements, these LSPR-based measurements of ligand adsorption, surface stability, and cleaning provide the basis for the experiments described below.

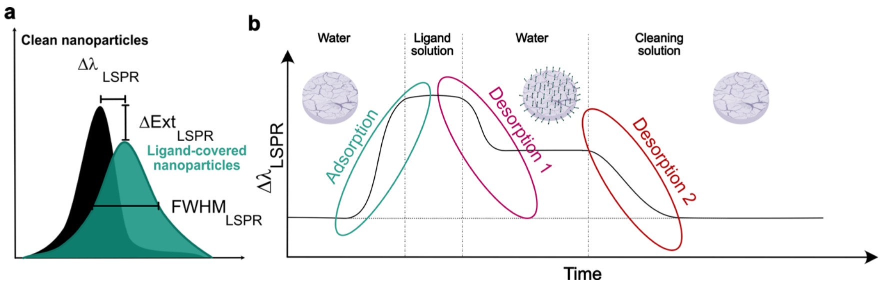

Figure 5-2. ***Schematic of the workflow developed in this thesis to monitor and characterize by LSPR sensing the ad/desorption of ligand molecules onto/from the surface of metal nanoparticles.*** *a) Schematic depiction of the UV-visible extinction spectra of the clean ligand-free nanoparticles in black and after ligand adsorption in green. The ligand-adsorption is expected to induce a distinct and measurable change to the LSPR peak in the spectrum. Specifically, to quantitatively extract these changes to the LSPR peak, three parameters are monitored during the ad/desorption experiment: (i) spectral centroid shift as defined by Dahlin et al*[127] *($\Delta\lambda_{LSPR}$), (ii) change in extinction at LSPR peak maximum (ΔExt_{LSPR}) and (iii) Full-Width-Half-Maximum of the LSPR peak ($FWHM_{LSPR}$). b) $\Delta\lambda_{LSPR}$ is monitored over time when the nanoparticles are exposed to a series of solutions. During ligand solution exposure, $\Delta\lambda_{LSPR}$ increases, i.e., shifts to longer wavelengths, due to a change in the immediate surroundings of the nanoparticles, where the rate of change of $\Delta\lambda_{LSPR}$ reveals the kinetics of adsorption until a steady state is reached where $\Delta\lambda_{LSPR}$ no longer changes. As the next step, the sample is exposed to a tailored cleaning solution which desorbs the ligands and induces a negative $\Delta\lambda_{LSPR}$, i.e., a shift to shorter wavelengths of the LSPR peak, to finally recover the original LSPR peak position in water that reflects the clean nanoparticle surface.*

5.1 CTAB Adsorption Experiments

To practically implement the experimental concept outlined in **Figure 5-1**, I fabricated arrays of Pt nanoparticles on fused silica substrates using Hole-mask Colloidal Lithography (HCL)[99], as described in **Chapter 4**. This yielded quasi-random arrays of disk-like particles with well-defined average diameter of 140 nm and height of 25 nm on 9 x 9 mm^2 fused silica support, hereafter referred to as the chip.

To expose such a chip to CTAB solutions at systematically varied bulk concentrations, I mounted it in the flow cell of an Insplorion XNano system schematically illustrated in **Figure 5-3**. The flow cell is constructed from titanium, providing chemical inertness and robustness against corrosion and oxidation. At its center, the cell contains a 10 mm × 10 mm chamber designed to accommodate the chip with the Pt nanoparticle array. Liquids are delivered to the flow cell using a peristaltic pump operated at a flow rate of 60 μL min^{-1} and through Tygon tubing connected to the flow cell inlet. A transparent sapphire window seals the flow cell on one side and the sample chip on the other, separated by a Kalrez gasket. This enables optical access to the chip and optical transmission measurements in the visible spectral range using optical fibers coupled to a halogen lamp (Avantes AvaLight-HAL-S) and a fixed-grating spectrometer (Avantes AvaSpec-HS-TEC) to perform nanoplasmonic sensing measurements. The spectra are recorded at 2 fps and have an optical window of 400 to 1000 nm. The liquid volume of the flow cell chamber is approximately 4 μL. Furthermore, the flow cell is equipped with a heating element and a thermocouple connected in a feedback loop to maintain a constant cell temperature. For all experiments, the measurement cell was held at 24.5 °C, while the solutions in the external reservoirs were maintained at 36 °C. The intentional temperature gradient between the solution reservoirs and the flow cell serves to reduce the formation of gas bubbles within the measurement cell. This is motivated by the fact that the solubility of gases in liquids decreases with increasing temperature[133]. Hence, heating the solution promotes degassing prior to entering the reactor. Subsequent cooling of the liquid upon entering the nanoreactor increases gas solubility, facilitating re-dissolution of any residual bubbles. However, despite these precautions, gas bubbles occasionally formed during measurements, necessitating frequent repetition of the experiment. Measurements affected by either bubbles or leaks were discarded.

To prepare for a measurement the sample chips were piranha solution (1:3 30% H_2O_2: 99% H_2SO_4) cleaned for 5 minutes and subsequently stored in MilliQ water for one day. Prior to each adsorption experiment, a borohydride cleaning step was also performed (see below for a study of its efficiency), it entailed sample immersion for 35 min in a 50 mM $NaBH_4$ solution prepared in a 1:1 ethanol:water mixture, followed by 10 min in a 1:1 ethanol:water mixture and finally at least 5 min in water. Borohydride ions are known to displace surfactant molecules adsorbed on metal surfaces, thereby enabling effective ligand removal[134,135]. As the next step, I placed a reference fused silica chip without nanoparticles in the flow cell to acquire reference optical spectra necessary for the plasmonic sensing experiment. Subsequently, I pumped heated water through the flow cell to first record a dark reference spectrum with a metal piece blocking the light source and secondly a bright reference spectrum with the light path unobstructed. These spectra from here forward refer to as the "dark reference spectrum" and the "bright reference spectrum", respectively. As the next step, I then mounted the cleaned Pt nanoparticle sample chip, again pumped heated water through the flow cell and acquired the plasmonic sample spectrum according to:

$$\mathrm{T} = \frac{\text{Sample spectrum} - \text{Dark spectrum}}{\text{Bright spectrum} - \text{Dark spectrum}} \tag{5.1}$$

$$\mathrm{E} = 1 - \mathrm{T} \tag{5.2}$$

where T is the transmittance and E is the extinction.

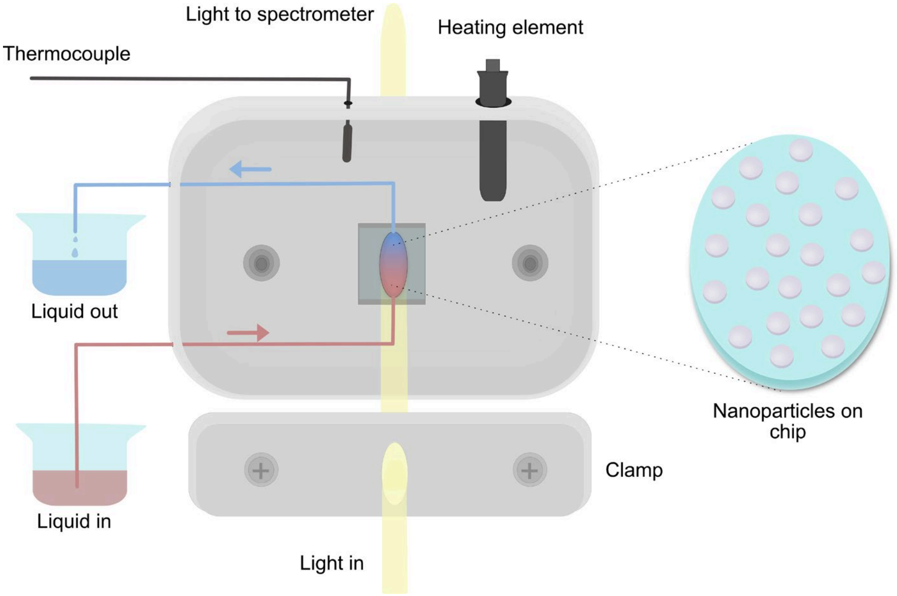

Figure 5-3. ***Schematic cross section of the set-up used for the CTAB adsorption kinetics measurements on Pt nanoparticle arrays.*** *The flow cell holds the chip and allows the continuous flow of liquids over it, while at the same time enabling continuous nanoplasmonic sensing experiments via optical transmission spectroscopy measurements in real time. The temperature is kept constant by using the heater element connected in a feedback loop to the thermocouple. Other parts of the set-up are omitted in the schematic for simplicity, which include holders, optical fibres, and collimating lenses.*

For the entire subsequent CTAB adsorption experiment, I kept the CTAB solution at 36 °C on a hotplate and the flow cell at 24.5 °C. First, I pumped water through the flow cell for 30 min to establish a stable baseline of the plasmonic $\Delta\lambda_{LSPR}$, signal that represents the initial clean surface state of the Pt nanoparticles. Subsequently, I pumped the CTAB solution of a given bulk concentration through the flow cell for 30 min (or longer if desired), while continuously monitoring the plasmonic signal. As the final step, I switched back to pumping water through the flow cell to rinse away any loosely bound CTAB molecules from the nanoparticle surface.

It is here interesting to discuss an example experiment in more detail and for this purpose I chose the adsorption and desorption of 70 mM CTAB on Pt nanoparticles (**Figure 5-4**). Specifically, I plot the time evolution of the plasmonic sensing signal divided into three widely used descriptors of the LSPR peak, namely the spectral shift of the peak maximum, $\Delta\lambda_{LSPR}$, as obtained when using the formalism introduced by Dahlin et al.[127]; the full-width-at-half-maxiumum of the LSPR peak, $FWHM_{LSPR}$, and the change in extinction at the peak maximum, ΔEXT_{LSPR}. Evidently, $\Delta\lambda_{LSPR}$ shifts to longer wavelengths upon exposure to CTAB. This can be understood as the formation of a thin layer on the Pt nanoparticles that has a higher refractive index than the surrounding water medium according to **equation 2.10** introduced in **Chapter 2**:

$$\lambda_{\mathrm{LSPR}} = \lambda_{\mathrm{p}}\sqrt{2\,\varepsilon_{\mathrm{d}} + 1}$$

where $\lambda_p$denotes the plasma wavelength and ε_d is the dielectric function of the surrounding medium. Interestingly, focusing first on the adsorption part of the $\Delta\lambda_{LSPR}$ time trace, the red-shift is not monotonous (or e.g. simply Langmuirian) but exhibits a distinct feature after about 50 seconds (**Figure 5-4b**). A similar feature is also seen in the $FWHM_{LSPR}$ trace and coincides with a distinct peak in the ΔEXT_{LSPR} trace. While it at this point is not fully clear what process that causes this feature, we speculate that it may correspond to either restructuring of the already adsorbed monomers[136] or, since 70 mM concentration is significantly above the CMC, that it is indicative of micelle-dominated adsorption, which either collapse into a mono- or bilayer film or are progressively replaced by adsorbing monomers.

A more detailed discussion of the adsorption process spanning bulk solution CTAB concentrations from 0.01 mM to 70 mM is found in **Paper I**.

Turning now to the water rinsing step, we notice that also here, the response of all three plasmonic parameters is non-monotonous (**Figure 5-4c**). Specifically, a distinct peak feature occurs after again approximately 50 s. While again not explicitly clear what mechanistically causes this effect, it likely indicates a multi-step desorption process of loosely bound CTAB molecules, e.g., via the transient formation of micelles on the surface, which could explain the transiently increased ΔEXT_{LSPR} signal as a consequence of these micelles scattering light efficiently. A deeper discussion is again to be found in **Paper I**. Finally, we also notice that the $\Delta\lambda_{LSPR}$ signal is not completely reversible after the water rinsing step, i.e. $\Delta\lambda_{LSPR} \neq 0$. This indicates that a certain amount of CTAB remains on the Pt nanoparticle surface, as expected. To further corroborate this result, we executed Time of Flight- Secondary Ion Mass Spectrometry (ToF-SIMS) as discussed in the next sub-chapter.

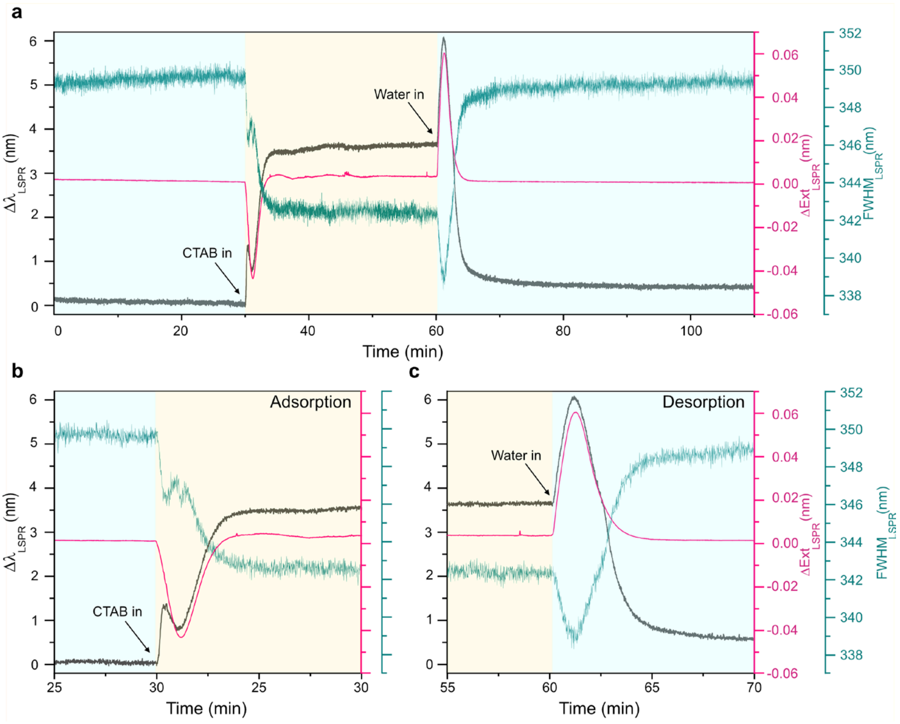

Figure 5-4. ***Representative nanoplasmonic sensing experiment of CTAB adsorption onto Pt nanoparticles from a 70 mM solution.*** *(a) Overview of the entire experiment during which the sample first is flushed with MilliQ water (blue shading) to establish a stable signal baseline in clean surface conditions, followed by the exposure to 70 mM CTAB solution for 30 min (yellow shading), prior to a 50 min rinsing step in again MilliQ water. The spectral shift of the peak maximum, $\Delta\lambda_{LSPR}$, as obtained when using the formalism introduced by Dahlin et al.* [127]*; the full-width-at-half-maximum of the LSPR peak, $FWHM_{LSPR}$, and the change in extinction at the peak maximum, ΔEXT_{LSPR} are extracted as peak descriptors over time. b, c) Zoom-ins on the CTAB adsorption and rinsing sections of the experiment, respectively. They reveal multiple step- and peak-like features which we tentatively attribute to restructuring processes within the adsorbed CTAB layer* or *micelle-dominated adsorption, which either collapse into a mono- or bilayer film or are progressively replaced by adsorbing monomers.*

5.2 Wet-Chemical Removal of Surfactants from a Nanoparticle Surface

As outlined in **Figure 5-1**, the experimental strategy developed in this thesis relies on repeatedly investigating the same lithographically fabricated catalyst nanoparticles under ligand-free conditions, after surfactant exposure, and again following chemical ligand removal. A central prerequisite for this approach is therefore a cleaning procedure capable of efficiently removing adsorbed surfactants while preserving nanoparticle morphology and surface chemistry as good as possible. This requirement is particularly important when evaluating catalytic activity, since cleaning-induced restructuring may otherwise obscure surfactant-related effects.

Common approaches for removing organic ligands from metallic nanostructures include UV–ozone exposure, oxygen plasma treatment, chemical oxidation, and high-temperature calcination[43]. Although highly effective at decomposing organic residues, these treatments frequently introduce oxidation, defect formation, or thermally driven restructuring of nanoscale catalysts. Plasma and ozone treatments promote oxide growth and surface roughening, whereas calcination can induce sintering, recrystallization, or support–particle interactions driven by enhanced surface diffusion at elevated temperatures[109,137]. Such irreversible changes are undesirable in the present work, where catalytic behaviour must be compared on the same nanoparticle population before and after surfactant adsorption.

I have therefore developed a mild wet-chemical protocol based on sodium borohydride ($NaBH_4$) dissolved in a 1:1 ethanol–water mixture[138,139]. In this protocol, sodium borohydride acts as a strong reducing agent capable of displacing adsorbed molecular species through hydride-mediated weakening of ligand–surface interactions and competitive adsorption at metallic interfaces, while simultaneously maintaining reducing conditions that suppress oxide formation during treatment[109,138]. The presence of ethanol plays a complementary role by modifying surfactant aggregation behaviour in solution. Alcohol co-solvents weaken hydrophobic chain packing and reduce aggregation stability of ionic surfactants such as CTAB in mixed solvent environments, thereby promoting dissolution of displaced surfactant assemblies and suppressing re-adsorption at the interface[113,115,118,140].

In my experiments, I performed this cleaning by immersing the samples in freshly prepared 50 mM $NaBH_4$ solution in 50:50 ethanol:water for 35 min under ambient conditions. During this step, reducing ligand displacement occurs at the metal interface while simultaneous destabilization of CTAB assemblies in the mixed solvent environment facilitates their transfer into solution[138,140]. The reducing environment further suppresses oxidation of the Pt surfaces during treatment. Following borohydride exposure, I transferred the samples to a $NaBH_4$-free 50:50 ethanol:water mix for 10 min. This intermediate rinsing step removes displaced surfactant molecules and reaction by-products remaining near the interface while maintaining favorable solvation conditions that prevent re-aggregation or re-adsorption of partially detached CTAB assemblies[115,140]. Subsequently, I rinsed in ultrapure water for at least 5 min to remove residual borohydride species and solvent impurities, thereby preventing continued reductive reactions and restoring aqueous surface conditions compatible with subsequent adsorption experiments[138]. Finally, I dried the samples under a nitrogen stream and stored under ambient laboratory conditions.

To evaluate the effectiveness of this cleaning protocol, as well as the selective adsorption of CTAB to Pt rather than the fused silica support, I performed time-of-flight secondary ion mass spectrometry (ToF-SIMS)[141] experiments. ToF-SIMS is a highly surface-sensitive analytical technique capable of providing spatially resolved chemical information from the outermost molecular layers of solid surfaces. I employed Bromide ion fragments (Br^-) as a quantitative marker for CTAB adsorption due to their direct association with the surfactant counterion and minimal contribution from background contamination, where common contaminants are hydrocarbons, sodium, chlorine and silicones[141]. To test the selective adsorption of CTAB onto Pt rather than the fused silica support used in my Pt nanoparticle experiments, I prepared a sample onto which I evaporated a 25 nm thick Pt film and on which I masked parts of the surface to create a distinct interface between the Pt film and the fused silica support. After cleaning in Piranha solution and immersion in water for 24 h, I exposed this thin film sample to 0.7 mM CTAB solution for 30 min followed by rinsing in MilliQ water for 30 min. Subsequent ToF-SIMS analysis of a 300 x 300 μm^2 area of the sample comprising a part of the Pt film and a part of bare fused silica reveals a strong Br^- signal from the area on which the simultaneously measured Pt^- signal confirms that it corresponds to the area of the Pt film (**Figure5-5a**). This measurement thus corroborates the selective adsorption of CTAB to Pt over the fused silica substrate.

Having established this selectivity, I nanofabricated two chips decorated with Pt nanodisk arrays fabricated by HCL on fused silica, featuring 140 nm disk diameter, 25 nm height as in all other samples I have used for my CTAB adsorption experiments. Subsequently, I also cleaned them in Piranha solution, immersed them in water for 24 h, and exposed them to 0.7 mM CTAB solution for 30 min followed by rinsing in MilliQ water for 30 min. As the last step, I exposed one of the chips using the $NaBH_4$ cleaning method I described above, to remove CTAB prior to ToF-SIMS analysis of both chips (**Figure 5-5b)**. Evidently, on the CTAB covered chip strong Br^- signal is recorded on Pt^-disk covered regions, whereas a scratch on the sample where Pt disks have been scraped off (dark-blue streak) is essentially CTAB-free. Furthermore, and as the key result, the $NaBH_4$ cleaned chip exhibits negligible Br^- signal (i.e., the signal is reduced by 95.6 %), which confirms the effectiveness of the developed $NaBH_4$ cleaning procedure.

As a last step to not only demonstrate the effectiveness of the cleaning recipe but to also confirm its mild nature in terms of (not) altering the Pt nanoparticles, I carried out catalysis experiments using the same reaction discussed in detail in **Section 5.4** and **Paper I**, i.e., the catalytic oxidation of ascorbic acid into dehydroascorbic acid on Pt[142]. Pt nanoparticles catalyze the oxidation of ascorbic acid in the presence of dissolved oxygen, leading to a decrease of the characteristic absorption band at 247 nm. The absorbance peak was quantified by Gaussian fitting to extract the peak amplitude as a function of time, enabling robust determination of reaction kinetics while minimizing baseline variations and spectral noise. Tracking the time evolution of this absorbance therefore provides a direct measure of catalytic activity. Catalytic oxidation was monitored in a closed reaction chamber with a volume of 56.5 μL, consisting of a clean glass slide without nanoparticles mounted against the nanoparticle chip and separated by an O-ring defining the liquid compartment. The chamber was completely filled with freshly prepared 735 μM ascorbic acid solution, with no additional oxygen gas bubbling and sealed prior to measurement. An identical chamber filled with water, and with no nanoparticles on the fused silica was used for online referencing. UV–visible absorption spectra were recorded over a wavelength range of 175–800 nm at a scan rate of one spectrum per minute at room temperature. Prior to the first measurement, the nanoparticle chip was cleaned in piranha solution for 5 min, stored in MilliQ water for 24 h, and subsequently subjected to the sodium borohydride cleaning protocol. Immediately after cleaning, the chip was mounted in the reaction chamber and catalytic activity was monitored for one hour. Following the measurement, the chip was rinsed in water to remove residual ascorbic acid and reaction products before immersion in 0.5 mM CTAB solution for 30 min, followed by rinsing in water for 30 min. A catalytic measurement after CTAB exposure (not shown here) was subsequently performed. After an additional water rinse for 20 min, the chip was cleaned again using the sodium borohydride protocol and the catalytic measurement was repeated under identical conditions.

Using this experimental scheme I then compared the time evolution of the absorbance value of the ascorbic acid absorption band at 247 nm for: (i) an as-nanofabricated and Piranha- plus subsequently $NaBH_4$-cleaned Pt nanoparticle chip; (ii) the same chip after exposure to a 0.5 mM CTAB solution for 30 min and subsequent $NaBH_4$ cleaning (**Figure 5-5c**). Evidently, the two-time traces are close to identical and thus corroborate (i) that the $NaBH_4$ cleaning recipe indeed removes CTAB from the Pt nanoparticle surfaces and (ii) does so in a very mild way, i.e., without structurally significantly altering the particles. Taken together, these experiments demonstrate that my cleaning procedure efficiently regenerates Pt nanoparticle surfaces to their pristine state, notably without significant structural modification, after exposure to CTAB. Therefore, it constitutes a key ingredient to the overall experimental concept developed in this thesis.

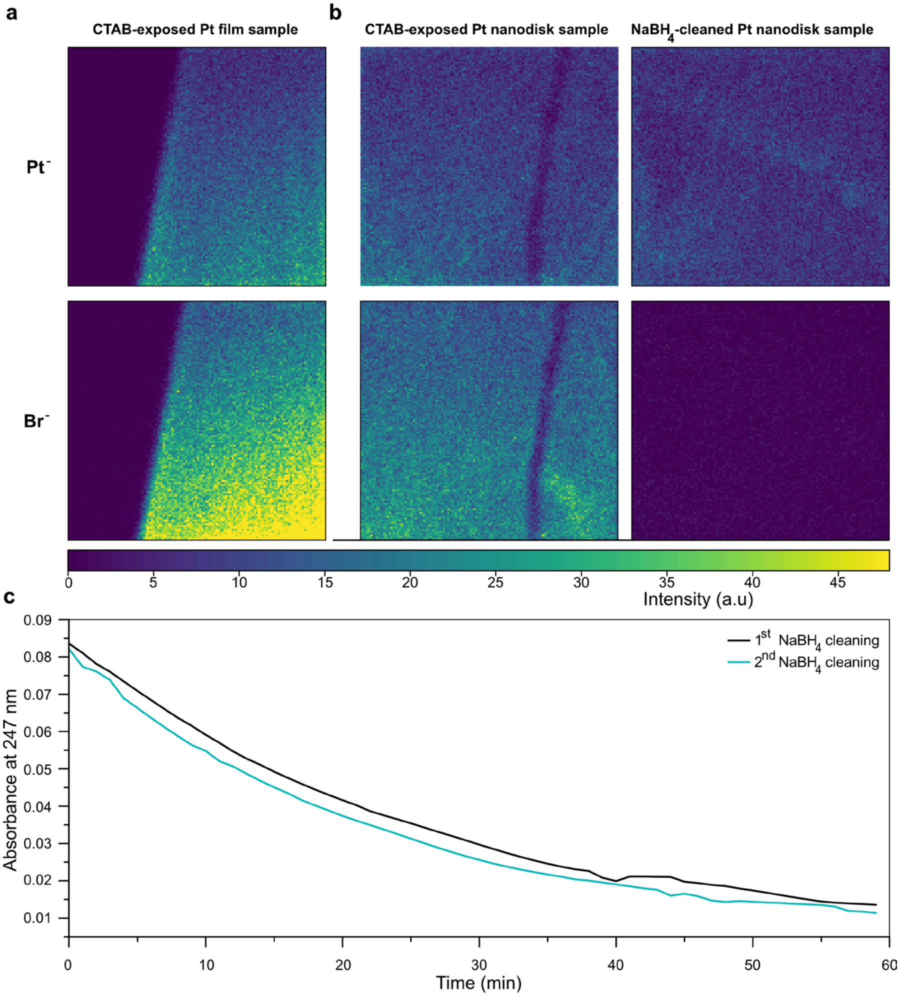

Figure 5-5. ***ToF-SIMS and catalytic assessment of selective CTAB adsorption to Pt and the $NaBH_4$ cleaning recipe for CTAB removal from Pt surfaces.*** *a) ToF-SIMS intensity maps for Br^- and Pt^- ions recorded from a sample partially covered with a 25 nm thick Pt film and partly exposing the fused silica support after exposure to 0.5 mM CTAB solution for 30 min. Evidently, the Br^- signal stems only from the part of the sample covered by the Pt film. This corroborates the preferential adsorption of CTAB on the Pt surface compared to the fused silica support. The depicted area of 300 x 300 μm^2 was scanned 380 times. b) ToF-SIMS intensity maps for Br^- and Pt^- ions recorded from a Pt nanodisk array sample after exposure to 0.5 mM CTAB*

solution for 30 min (left column) and an identical Pt nanodisk array sample first exposed to 0.5 mM CTAB solution for 30 min and then cleaned using the NaBH4 cleaning procedure I have developed in this thesis (right column). Evidently, the $NaBH_4$ cleaned chip exhibits negligible Br^- signal (i.e., the signal is reduced by 95.6 %), which confirms the effectiveness of the developed $NaBH_4$ cleaning procedure. The dark-blue "streak" on the CTAB-covered sample corresponds to a scratch where the Pt nanodisk have been scraped off. The depicted area of 300 x 300 μm^2 was scanned 380 times. c) Time evolution of the absorbance at the ascorbic acid peak (247 nm) extracted by Gaussian fitting during catalytic oxidation on Pt nanoparticles monitored by UV–visible spectroscopy. The black trace corresponds to a Piranha-cleaned nanoparticle chip followed by $NaBH_4$ cleaning. The cyan trace corresponds to the same chip after exposure to 0.5 mM CTAB for 30 min followed by $NaBH_4$ cleaning prior to measurement. The decrease in absorbance reflects catalytic oxidation of ascorbic acid on the Pt nanoparticle surface.

5.3 ToF-SIMS Analysis across Four Concentrations of CTAB

ToF-SIMS is a highly surface-sensitive analytical technique in which a focused, pulsed primary ion beam (e.g., Bi^+, Bi^{3+}, Ga^+, or Ar^+) is used to bombard a region of interest[141]. The impact of the primary ions induces a fragmentation cascade within the uppermost atomic layers of the sample, resulting in the emission of neutral species and secondary ions that may be either positively or negatively charged. These secondary ions are accelerated into a flight tube, where their mass-to-charge ratio is determined from their time of flight to the detector. Measurements are performed under ultrahigh vacuum conditions to maximize the mean free path of the emitted ions. ToF-SIMS enables two-dimensional chemical mapping of the sample surface and, through sequential sputtering, also depth-resolved chemical analysis. In the present study, a Bi_3^+ primary ion source was used to quantify the amount of

CTAB adsorbed onto my Pt nanoparticle chips both directly after the adsorption step and after rinsing with water.

For these experiments, I prepared eight nanoparticle chips in a single nanofabrication batch. All chips were first cleaned using piranha solution, followed by the borohydride cleaning sequence detailed above. Four CTAB solution concentrations were investigated: 0.35 mM, 0.70 mM, 2.00 mM, and 40.00 mM. This means that two concentrations were below the CMC (reported to be approximately 1 mM and two above the CMC[119]. For each concentration, two chips were subjected to adsorption experiments in the flow cell setup as described above, while measuring their $\Delta\lambda_{LSPR}$ response. One of the two chips dedicated for each concentration underwent the full adsorption cycle consisting of water flushing for 20 min, CTAB exposure for 30 min, and a water rinse for 30 min. For the second chip, the final water rinsing step was omitted to thereby preserve the loosely bound CTAB molecules on the surface. After completion of CTAB exposure/rinsing sequence, all chips were dried under a nitrogen flow and stored for 8 h before being loaded into the ToF-SIMS vacuum chamber.

The obtained and combined results from the CTAB adsorption and rinsing experiments with $\Delta\lambda_{LSPR}$ readout and the corresponding ToF-SIMS analysis are presented in **Figure 5-6**. As the first observation, we see that $\Delta\lambda_{LSPR}$ observed during CTAB exposure increase systematically with CTAB concentration in the bulk solution (**Figure 5-6a**), indicating a larger amount of CTAB adsorbed on the surface prior to rinsing for higher CTAB concentration in solution. Interestingly, however, while $\Delta\lambda_{LSPR}$ after water rinsing increases from 0.35 mM to 0.70 mM CTAB, they decrease markedly at higher concentrations, indicating that a larger fraction of the adsorbed CTAB becomes weakly bound and is removed during rinsing (**Figure 5-6a,b**). This interpretation is supported by the ToF-SIMS analysis of Br^-

signals (**Figure 5-6c, d**). Unwashed samples show increasing Br^- counts with CTAB concentration, whereas washed samples exhibit a maximum for 2.00 mM followed by a sharp decrease at 40.00 mM. Together, the plasmonic and ToF-SIMS results indicate that although higher CTAB concentrations lead to greater overall adsorption in solution, they promote the formation of more weakly bound surfactant assemblies that are more readily removed during water rinsing. Concentration-dependent cooperative adsorption of CTAB leading to the formation of multilayer or aggregate-like interfacial structures has previously been reported for negatively charged mica surfaces, where adsorption proceeds via hemimicellar and bilayer-type organization below and near the critical micelle concentration (CMC)[143]. Complementary QCM-D studies on gold further demonstrate that increasing CTAB concentration can produce more dissipative and dynamically reorganizing adsorbed layers, consistent with reduced interfacial rigidity[136]. Direct comparison must nevertheless be made with caution, as adsorption on mica and oxide substrates is primarily governed by electrostatic interactions with charged surfaces, whereas CTAB adsorption on metallic Pt nanoparticles may additionally involve bromide-mediated adsorption and metal-specific interfacial interactions.

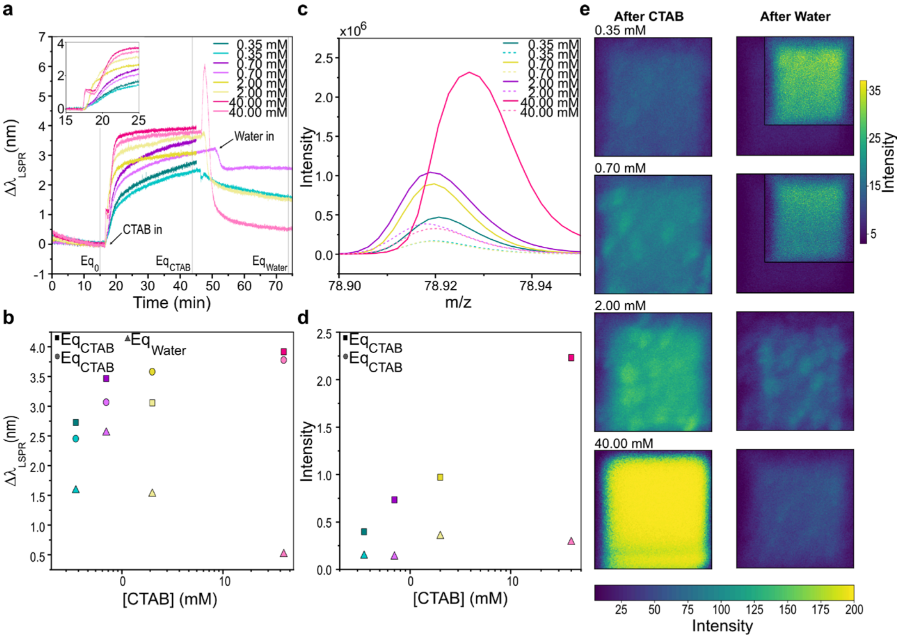

Figure 5-6. ***Correlated plasmonic sensing and ToF-SIMS measurements for four different CTAB solution concentrations: 0.35 mM, 0.70 mM, 2.00 mM, 40.00 mM .*** *a) Time-resolved $\Delta\lambda_{LSPR}$ response for the eight measured samples upon exposure to CTAB solution at the indicated concentrations. After CTAB exposure, four of the samples are rinsed with water. Eq_0 denotes the stable equilibrium baseline time stamp at which the CTAB solutions were introduced. Eq_{CTAB} denotes the time stamp at which the later rinsing step was initiated. Eq_{water} denotes the time stamp at which water rinsing was terminated. The inset shows a magnified view of the regime of fast adsorption, where the initial adsorption rate increases with CTAB concentration in solution. b) $\Delta\lambda_{LSPR}$ values extracted at Eq_{CTAB} correspond to samples unrinsed (□) and rinsed with water (○) after CTAB exposure, and Eq_{Water} (Δ plotted as a function of CTAB concentration in solution. c) ToF-SIMS Br^--spectra for rinsed (dashed lines) and unrinsed (solid lines) samples. Clearly, the unrinsed samples exhibit significantly higher Br^- counts across the board compared to their rinsed counterparts, corroborating the effective washing of loosely bound CTAB molecules during the rinsing step. Integration of the Br^- peak area yields Br^- signal reductions of 64.0%, 81.8%, 63.8%, and 85.8% for 0.35 mM, 0.70 mM, 2.00 mM, and 40.00 mM CTAB, respectively. d) Integrated Br^- counts as a function of*

CTAB concentration for rinsed and unrinsed samples. For the unrinsed samples, Br^- counts increase monotonically with solution CTAB concentration. For rinsed samples, however, the Br^- signal increases up to 2.00 mM and decreases sharply at 40.00 mM, indicating a reduction in the fraction of strongly bound CTAB at high concentrations. e) ToF-SIMS Br^- intensity maps (100 µm × 100 µm) for all eight samples over 200 scans. The first column shows increasing Br^- signal intensity with increasing CTAB concentration for unrinsed samples, while the second column shows a pronounced reduction in Br^- signal after water washing. Localized Br^- intensity maxima are attributed to preferential CTAB adsorption on Pt nanoparticle aggregates relative to the glass substrate. For the rinsed 0.35 mM and 0.70 mM samples, additional inset maps with a shared rescaled colour bar are included to enhance visibility of the weak residual Br^- signal.

5.4 The Impact of CTAB on Catalytic Decomposition of Ascorbic Acid on Pt Nanoparticles

Following the establishment of reproducible CTAB adsorption and efficient ligand removal procedures described in the previous sections, the experimental workflow was extended toward catalytic investigations. The aim of these experiments was to assess how controlled ligand coverage influences the catalytic performance of Pt nanoparticle ensembles. By combining adsorption–removal cycles with repeated catalytic measurements performed on the same nanoparticle chip, changes in catalytic activity could be directly correlated with defined surface coverages.

Ascorbic acid (vitamin C, denoted by AH_2 in this thesis) is a biologically important antioxidant that protects living systems against oxidative damage caused by reactive oxygen species[144]. In aqueous environments containing dissolved oxygen, AH_2 undergoes oxidation through a sequence of electron transfer reactions (**equation 5.3**) involving the ascorbate monoanion (AH^-)

and the ascorbate radical intermediate ($A^{\bullet -}$), ultimately forming dehydroascorbic acid (A^{2-}) and subsequent degradation products[142,145,146].

$$AH_2 \rightleftharpoons AH^- \longrightarrow A^{\bullet -} \rightleftharpoons A^{2-} \tag{5.3}$$

The oxidation process can proceed via uncatalyzed autoxidation pathways but is strongly accelerated in the presence of transition metals or catalytically active surfaces[146]. Noble metal nanoparticles, in particular platinum, have been shown to exhibit oxidase-mimetic activity toward ascorbate, promoting oxygen reduction coupled to substrate (here ascorbic acid) oxidation[147]. Therefore, the catalytic activity of Pt nanoparticles provides a sensitive probe for investigating how surface-bound ligands influence accessibility of active sites. Spectroscopically, AH_2 and AH^- exhibit characteristic ultraviolet absorption bands at approximately 247 nm and 264 nm respectively. Monitoring the temporal evolution of these absorbance features enables quantitative tracking of the concentrations of these two acid–base forms during the reaction[142]. In this way, the UV–vis analysis probes the depletion of AH_2 in solution and the evolution of the AH_2/AH^- distribution under oxidizing conditions.

Catalytic measurements could not be performed directly in the flow cell used for CTAB adsorption experiments. The continuous liquid flow inherent to the flow cell configuration prevents stable concentration control, as reactants and products continuously diffuse into and out of the measurement region. This limitation becomes particularly critical for catalytic reactions proceeding on minute-to-hour timescales, such as oxygen-driven ascorbic acid oxidation under ambient aqueous conditions[145,146]. Furthermore, the optical detection range of the setup is limited to wavelengths above approximately 400 nm, preventing access to the characteristic UV absorption bands[142] required to monitor AH_2 and AH^-.

Catalytic activity measurements were therefore performed using a UV–Vis spectrophotometer (Cary 5000), enabling measurements in a closed batch reactor geometry with fixed solution volume and well-defined optical path length. The reaction chamber consisted of the nanoparticle chip sealed against a fused silica cover plate using a chemically resistant FFKM O-ring and held together mechanically by a custom-made 3D-printed sample holder (**Figure 5-7**). Mechanical stability and compatibility with the cuvette holder of the spectrometer were achieved using the same custom-made 3D-printed sample holder. The cylindrical chamber had an inner diameter of 6 mm and a height of 2 mm, corresponding to a total reactant volume of 56.5 μL.

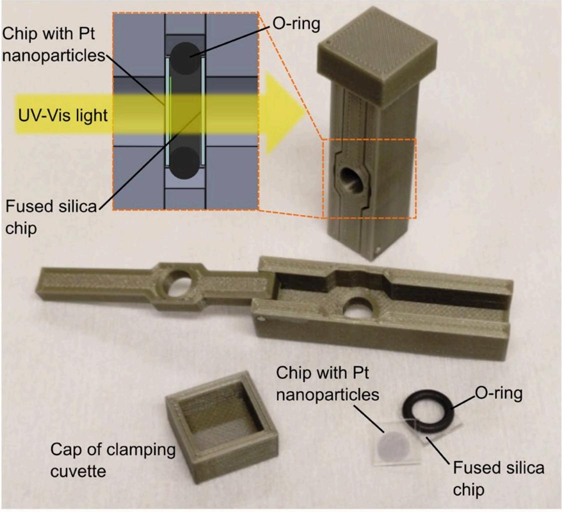

Figure 5-7. ***Schematic and photograph of the custom reaction chamber used for batch UV–Vis catalytic measurements.*** *The Pt nanoparticle chip (nanofabricated on fused silica) is sealed against a second fused silica chip using a chemically resistant FFKM O-ring, forming a confined reaction volume. The assembly is held together by a 3D-printed sample holder compatible with the cuvette compartment of the Cary 5000 UV–Vis spectrophotometer. UV–Vis light passes through the fused silica windows and the reaction volume, enabling time-resolved monitoring of ascorbic acid oxidation on the Pt nanoparticle surface under closed, fixed-volume conditions.*

To account for background absorption contributions arising from the fused silica substrates, solvent and optical interfaces, reference spectra were recorded using an identical reaction chamber assembled with a fused silica chip without nanoparticle deposition. The reference chamber was filled with ultrapure water and measured under identical experimental conditions. All catalytic spectra were referenced against this configuration to isolate absorbance changes originating solely from the reactants, products and nanoparticles. Pt nanoparticle chips were fabricated by hole-mask colloidal lithography as described in **Chapter 4**, but with the addition of a metal mask containing a circular aperture with a diameter of 6 mm used during the metal evaporation step. This step allows the nanoparticle chip to have a defined constant active catalytic area corresponding to the same area delimited by the O-ring.Prior to catalytic measurements, the nanoparticle chips were subjected to a multistep cleaning procedure to remove organic contaminants and residual ligands. Samples were first treated with freshly prepared piranha solution (1:3 30% H_2O_2: 99% H_2SO_4) for 5 min, followed by immersion in ultrapure water for 24 h. Subsequently, chemical reduction cleaning was performed by immersion for 35 min in 50 mM $NaBH_4$ prepared in a 1:1 ethanol-water mixture. The chips were rinsed for 10 min in 1:1 ethanol-water and finally for 5 min in ultrapure water. Immediately after completion of the borohydride cleaning step, catalytic measurements were performed to establish the ligand-free reference state. Surface modification was achieved by immersing the chip in 4 ml CTAB solutions of defined bulk concentration at 35 °C for 30 min. Afterwards, the sample was transferred to ultrapure water for 30 min to remove loosely bound surfactant molecules, reproducing the adsorption and rinsing conditions used in the flow cell adsorption experiments. Following catalytic measurements on CTAB-covered samples, the ligand layer was removed by repeating the $NaBH_4$ cleaning procedure described above, thereby regenerating the ligand-free surface. This adsorption–removal cycle was repeated for different CTAB bulk concentrations, allowing sequential catalytic measurements to be performed on the same nanoparticle ensemble under systematically varied surface conditions.

For catalytic experiments, freshly prepared aqueous 735 µM ascorbic acid solutions were introduced into the sealed reaction chamber immediately prior to measurement. Each catalytic experiment consisted of 60 consecutive

UV–Vis spectra recorded between 175 nm and 800 nm with a temporal resolution of 1 min per spectrum. Illumination was provided by a deuterium arc lamp for ultraviolet wavelengths and a tungsten halogen lamp for the visible regime.

Representative catalytic measurements obtained before and after CTAB adsorption from bulk concentrations of 70 mM are shown in **Figure 5-8**. The ultraviolet absorbance peaks corresponding to AH_2 and AH^- are located in close spectral proximity and partially overlap (**Figure 5-8a**), preventing direct extraction of individual peak intensities. To resolve this overlap, peak absorbances were determined using a MATLAB routine based on fitting a double-Gaussian model with fixed peak positions corresponding to the respective species. This fitting approach enabled robust separation of the spectral contributions from AH_2 and AH^- (**Figure 5-8b**). The oxidation of AH_2 was subsequently quantified by tracking the temporal evolution of the absorption bands at 247 nm and 264 nm assigned to AH_2 and AH^- respectively (**Figure 5-8c**). Each catalytic experiment required manual filling, assembly, and insertion of the reaction chamber into the spectrophotometer prior to data acquisition. Consequently, a finite and experiment-dependent delay occurred between the initial contact of the ascorbic acid solution (AH_2) with the Pt nanoparticle surface and the acquisition of the first UV–Vis spectrum. During this period, catalytic oxidation had already commenced, resulting in variations in the initial absorbance values recorded at the first measured time point. To enable direct comparison between experiments, time traces were aligned by extrapolating the fitted first-order decay function backward in time to compensate for variations in manual handling time prior to the first recorded spectrum. This procedure compensates for variations in handling time while preserving the intrinsic kinetic behaviour extracted from the exponential fits.

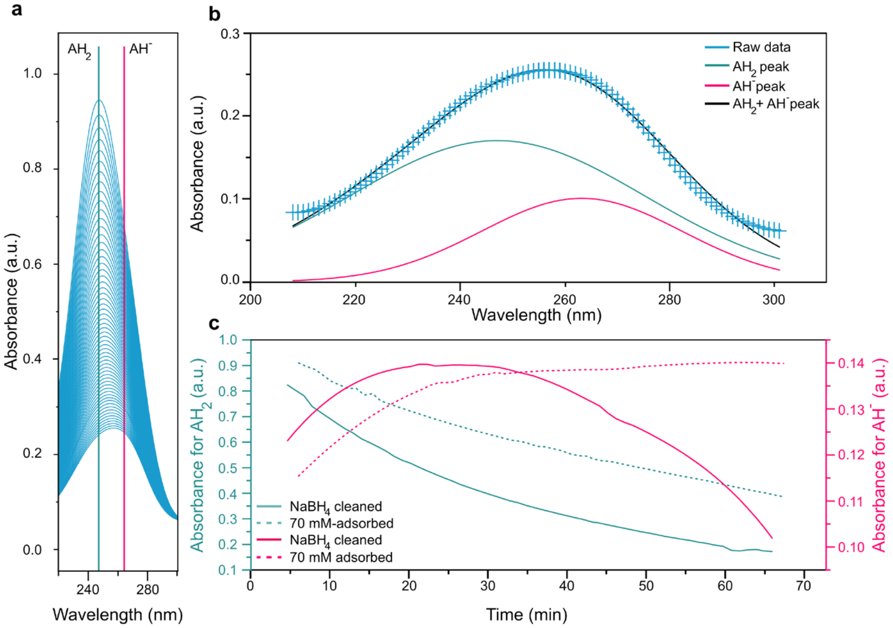

Figure 5-8. ***Catalytic oxidation of ascorbic acid on Pt nanodisk arrays (140 nm diameter, 25 nm height), comparing ligand-free nanoparticles with nanoparticles modified by adsorption from a 70 mM CTAB solution.*** *a) UV–Vis spectrum recorded at 64 min for the $NaBH_4$-cleaned sample, showing the overlapping absorption bands of AH_2 at 247 nm and AH^- at 264 nm. b) Representative double-Gaussian fit used to separate the AH_2 and AH^- contributions and extract individual peak absorbances. c) Time evolution of the extracted peak absorbances for ligand-free (black) and CTAB-modified (cyan) samples. Time traces were aligned by backward extrapolation of first-order fits to compensate for differences in handling time before acquisition of the first spectrum (see main text). Concentrations were calculated using the Beer–Lambert relation, molar absorptivities*[148] *of 6800 L mol^{-1} cm^{-1} for AH_2 and 16500 L mol^{-1} cm^{-1} for AH^-, and a 2 mm optical path length. CTAB-modified nanoparticles show slower AH_2 decay and greater accumulation of AH^- than ligand-free particles, for which the AH^- signal decreases after reaching a maximum at around 25 min, indicating reduced catalytic turnover and altered reaction selectivity.*

Compared to the ligand-free reference state, CTAB-modified nanoparticles exhibited a reduced catalytic activity, consistent with partial blocking of catalytically active surface sites by the adsorbed surfactant layer[45,109,124]. First-order exponential fitting of the decay of the AH_2 absorbance yielded an apparent reaction rate constant decrease from $k = 4.74 \cdot 10^{-4}\ s^{-1}$ to $k = 2.74 \cdot 10^{-4}\ s^{-1}$ after CTAB adsorption, corresponding to an approximately two-fold reduction in catalytic turnover. In addition to the reduced reaction rate, a pronounced change in reaction selectivity was observed. For ligand-free nanoparticles, the absorbance associated with the ascorbate monoanion (AH^-) increased to its maximum at 30 min and from then, the absorbance decreased continuously indicating further oxidation toward dehydroascorbic acid (A^{2-}) and subsequent degradation products. In contrast, CTAB-modified nanoparticles showed a substantially flatter AH^- absorbance evolution, indicating accumulation of this intermediate species during the reaction. This response suggests that CTAB adsorption not only decreases the number of accessible catalytic sites but also modifies the reaction pathway by inhibiting subsequent oxidation steps of the ascorbate intermediate. Such ligand-induced selectivity changes are consistent with reports demonstrating that surface-bound organic ligands can alter catalytic reaction pathways by sterically blocking active sites or modifying interfacial electron transfer processes[49,50,145,149].

Control experiments performed using nanoparticle-free reference chips showed only negligible changes in absorbance over the experimental time scale (**Supporting Information** of **Paper I**), confirming that the observed reaction acceleration originates from Pt nanoparticle catalysis rather than bulk autoxidation[146,149,150].

Taken together, these results demonstrate that controlled CTAB adsorption leads to both a measurable decrease in catalytic turnover and a modification of reaction selectivity in the ascorbic acid oxidation reaction. The simultaneous reduction in apparent rate constant and accumulation of the AH^- intermediate indicate that ligand adsorption affects not only the number of accessible active sites but also the interfacial reaction pathway. These findings establish a direct correlation between surface ligand coverage and catalytic response, thereby validating the experimental strategy employed to probe ligand–nanoparticle interactions under well-defined conditions.

6 Towards Single Nanoparticle Experiments

As discussed in detail in the **Introduction** of this thesis, there exist strong arguments for why detailed investigations of ligand adsorption on metal nanoparticles, and how such ligands impact heterogeneous catalysis, ideally would be carried out with single nanoparticle resolution. Therefore, as a first step in this direction, I will in this chapter present a first preliminary single-nanoparticle experiment that demonstrates the feasibility of resolving ligand adsorption at the level of an individual nanoparticle localized inside a nanofluidic channel. To do so, I apply the experimental scheme that I have developed in this thesis for measurements of this type at the nanoparticle ensemble level that I described in detail in **Chapter 5** and in **Paper I,** and I attempt to translate it to single nanoparticle experiments. As the second key ingredient, I attempt such an experiment in the setting of Nanofluidic Scattering Spectroscopy (NSS)[59,60,89,90,151]. This means, that the single nanoparticle of interest is placed inside a nanofluidic channel as discussed in detail below. This on one hand enables the accurate control of liquid flow to and from the nanoparticle[152] and on the other hand unlocks the possibility to quantitatively monitor not only the nanoparticle's intrinsic light scattering response during the process but also the light scattered from the nanochannel that hosts that particle and thereby gain insight into, for example, changes in composition/concentration of the solution after having interacted with the nanoparticle[59,60,89,90,151]. In this way, it is the long-term goal to be able to execute the experimental scheme introduced in **Figure 1-5** at the single nanoparticle level in a single experiment. For the proof of principle experiment I present below, I used single Au nanoparticles due to their superior light scattering properties compared to Pt[153].

6.1 Nanofluidic Chip Fabrication

The realization of measurements outlined above relies on nanofluidic chips that allow precise fluid handling, while maintaining optical access to the embedded nanoparticle. The fabrication of these chips is therefore a critical prerequisite and is described in detail below. These nanofluidic chips generically consist of inlets that connect the chip to a macroscopic liquid handling system, a microfluidic inlet system that transports the liquid to the nanofluidic system that is comprised of an array of parallel nanochannels, a microfluidic outlet system that transports the liquid that has been flushed through the nanofluidic system away from it to a second set of outlet reservoirs, and two separate reference fluidic systems used to correct for light intensity variations during NSS experiments **(Figure 6-1)**. By applying gas pressure to the inlet connections convective flow through such a chip is established.

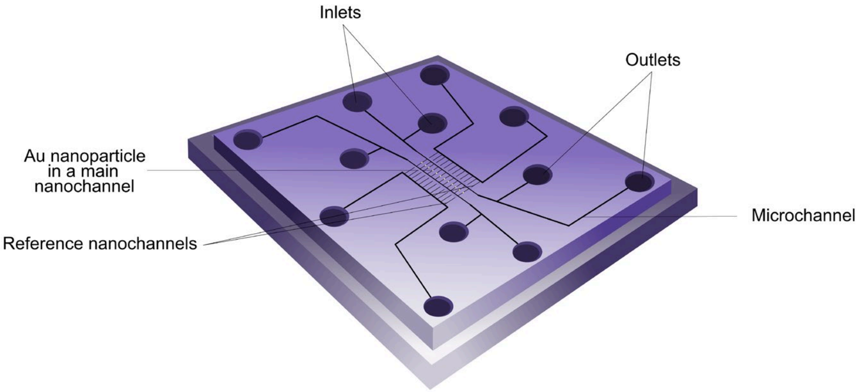

Figure 6-1. ***Rendition of a 12-inlet nanofluidic chip.*** *Twelve inlets are connected to three sets of twelve parallel straight nanochannels via four microchannels. The sample nanochannels in the center of the chip contain a single Au nanoparticle each*[154]**.**

The fabrication of such chips, decorated with single nanoparticles, is a complex multi-step process carried out in the MC2 micro- and nanofabrication facility at Chalmers by a nanofabrication expert in our group. I assisted this process during the design phase. The chips are fabricated on silicon wafers by combining thermal oxidation, electron-beam lithography, photolithography, dry etching, and wafer bonding. The process flow comprises wafer cleaning, thermal oxidation, nanochannel etching into SiO_2, nanoparticle fabrication inside the nanochannels, microchannel etching through the oxide and into silicon, access hole formation, and final bonding and dicing according to the following steps:

1. *Wafer cleaning*

   Silicon wafers with (100) orientation are cleaned using a standard RCA protocol. The wafers are treated in SC-1 (5:1:1 H_2O:NH_4OH:H_2O_2 at 80 °C) for 10 min and rinsed in deionized (DI) water. The native oxide is removed by a brief dip in 2% HF for 10 s, followed by a DI water rinse.

The wafers are subsequently treated in SC-2 (5:1:1 H_2O:HCl:H_2O_2 at 80 °C) for 10 min, rinsed in DI water, and spin-dried.

2. *Thermal oxidation*

A silicon dioxide layer is grown by thermal oxidation in a water-vapor atmosphere at 1050 °C. In this process, the nanochannels are fabricated in the thermally grown SiO_2 layer of approximately 280 nm is used. While optical interference effects are present already at this thickness, keeping the oxide relatively thin leads to more widely spaced oscillations in optical spectra, which facilitates interpretation compared to thicker oxides where oscillations become more closely spaced.

3. *Nanochannel etching in SiO_2 (Cr hard mask + EBL + RIE)*

Nanochannels are etched into the thermally grown SiO_2 layer to a target depth of ~200 nm using reactive ion etching (RIE) with a chromium hard mask. First, a ~20 nm Cr film is deposited onto the oxidized wafer. An electron-beam resist (ARP6200) is spin-coated on top, and the nanochannel layout is defined by electron-beam lithography followed by development in o-xylene. The resist pattern is transferred into the Cr layer by chlorine-based RIE (Cl_2). Residual resist is removed by an O_2 plasma clean. The patterned Cr hard mask is then used to transfer the nanochannel pattern into the SiO_2 layer using fluorine-based RIE (NF_3).

4. *Nanoparticle fabrication inside the nanochannels (lift-off)*

Nanoparticles are fabricated after nanochannel definition and prior to microchannel etching. A bilayer lift-off resist stack consisting of a copolymer base layer and PMMA is spin-coated onto the wafer and exposed by electron-beam lithography to define nanoparticle sites. After development, a thin metal film (typically Au or Pt) is deposited by physical vapor deposition. Lift-off is performed in Remover 1165, leaving metal nanoparticles at predefined positions within the nanofluidic structures.

5. *Microchannel etching (oxide opening + Si Bosch DRIE)*

The microfluidic channels are defined by optical lithography using a positive photoresist (S1813), typically patterned by direct laser lithography. The exposed SiO_2 is opened using fluorine-based RIE to create an etch mask. The microchannels are then etched into the silicon substrate to a depth of approximately 5 µm using a Bosch-type deep reactive ion etching (DRIE) process with a limited number of cycles.

6. *Fluidic access holes (inlets)*

To provide fluidic access between on-chip structures and macroscopic reservoirs, through-wafer access holes are etched by backside DRIE through the silicon substrate. In chip variants that require front-side access through the glass lid, access holes in the Borofloat lid can be produced at defined positions (e.g., by sandblasting). This option is only used for selected designs and is not part of the default flow.

7. *Lid bonding and dicing*

Prior to bonding, the processed silicon wafer is cleaned in SC-1 (5:1:1 $H_2O:NH_4OH:H_2O_2$ at 80 °C) for 10 min, rinsed in DI water, and dried with N_2. A 175 µm thick Borofloat 33 glass wafer is cleaned in the same manner. The silicon and glass wafers are activated by O_2 plasma treatment

(50 W RF power, 250 mTorr). Immediately after plasma activation, the wafers are brought into contact and manually pressed to form a pre-bond. Any visible voids are mechanically driven towards the wafer edge (e.g., using plastic tweezers) to improve bonding uniformity. The wafer stack is subsequently thermally bonded at 550 °C for 5 h and then diced into 52 individual chips for surfactant adsorption and catalysis experiments.

6.2 Proof-of-Concept Single Nanoparticle Experiment

As the first step of my proof-of-principle experiment, I mounted a nanofluidic chip in a dedicated sample holder described in detail in an earlier publication by our group[154]. This holder enables the mounting of the chip on an upright optical dark-field microscope (Nikon Eclipse LV150N) configured for both imaging and spectroscopy **(Figure 6-2)**[90]. For the dark-field illumination of the sample through a reflection-mode dark-field objective (50X), I used a LED lamp (Thorlabs Solis3C) with an output power of 4 W. In dark-field illumination, the sample is illuminated at an oblique angle such that only scattered light from the nanochannels and the embedded nanoparticle is collected by the objective, producing bright features against a dark background **(Figure 6-3a,b)**. For spectroscopic analysis of the scattered light, the microscope is equipped with a spectrometer that disperses the collected scattered light by a grating (SR-193I-A-SL with a 150 l/mm grating) onto a CCD camera (Andor Newton DU920P-BEX2-DD).

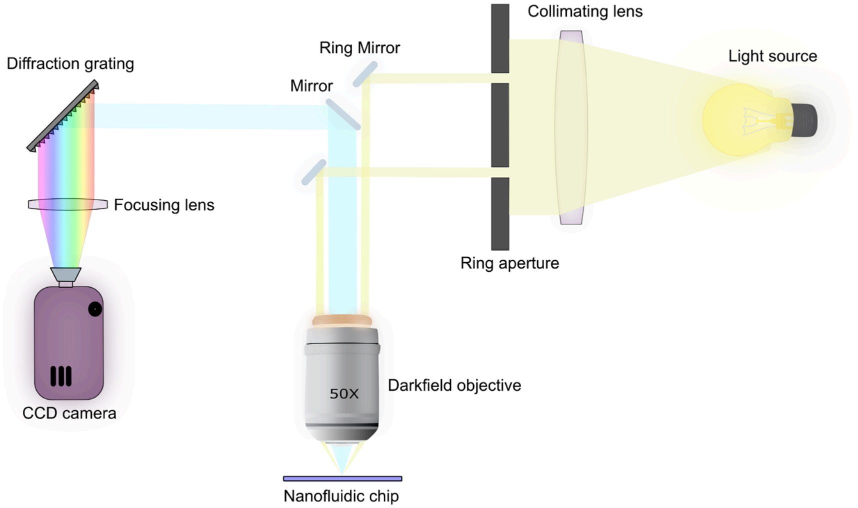

Figure 6-2. ***Schematic of the dark-field microscope configuration used for Nanofluidic Scattering Spectroscopy of CTAB adsorption on a single Au nanoparticle.*** *In this setup, an LED serves as the illumination source, and the emitted light is collimated before passing through a ring aperture that directs a hollow cone of light into the outer lenses of the dark-field objective. This geometry illuminates the sample at a shallow angle, such that only light scattered by the nanofluidic chip enters the central collection optics, producing high-contrast images against a dark background. A diffraction grating mounted on a rotating turret enables switching between imaging and spectroscopy modes. In the zeroth-order position, reflected light is directed to the detector for conventional dark-field imaging. When rotated to the first-order position, the scattered light is spectrally dispersed across the camera sensor, where calibrated pixel positions correspond to specific wavelengths, allowing acquisition of wavelength-resolved scattering spectra.*

Nanofluidic experiments were performed using a nanofluidic chip mounted in a custom-made chip holder ("chuck") that enables controlled liquid delivery and optical access during dark-field measurements (**Figure 6-3a,b**)[154]. Prior to surfactant adsorption measurements, the chip was cleaned by immersion in freshly prepared piranha solution for 5 min, followed by storage in ultrapure water for 24 h. The chip was then positioned inside a machined cavity of the aluminium frame of the chuck with the inlet openings facing upward, after which a transparent flow plate equipped with O-ring seals was secured on top using four screws tightened incrementally to ensure uniform sealing. Each inlet was connected to a metal cannula that terminated with a Luer-Lock coupling, allowing liquid loading via syringe and pressure control through external gas tubing. Nitrogen gas pressure supplied via a pressure controller (Fluigent) enabled selective actuation of individual inlets. Liquids introduced into the microchannels were driven towards the nanochannel region by pressure-assisted convection in combination with capillary forces, allowing controlled exchange of solutions inside the nanochannels, as previously demonstrated for nanofluidic scattering spectroscopy experiments[61,90,154]. Temperature control was provided by integrated Peltier elements incorporated into the aluminium frame of the chuck.

All the top six inlets in **Figure 6-3C** were filled with water and pressure was applied by using the connected gas tubes. The microchannels and nanochannels were wetted with MilliQ water to establish reproducible initial fluidic conditions. All measurements were performed with the chip and its holder at 30 °C to prevent CTAB crystallisation[120]. During measurements, the water in one microchannel of the central fluidic system was exchanged with heated 70 mM CTAB solution, while the opposing microchannel contained MilliQ water (**Figure 6-3c**). By selectively applying slight overpressure to the corresponding inlets, the liquid composition inside the nanochannels could be rapidly exchanged, enabling well-defined water–CTAB–water cycles analogous to the protocol established for Pt nanoparticle ensemble experiments (**Chapter 5**). In addition to the central sample nanochannel system with the Au nanoparticles, two independent reference nanochannel systems located on either side of the sample region were continuously maintained under water flow to provide stable optical reference signals[61,90,154].

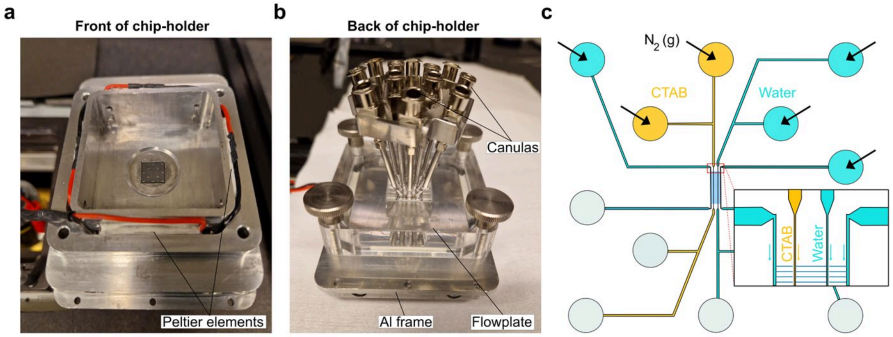

Figure 6-3. ***Nanofluidic chip holder and pressure-driven liquid exchange scheme used for single-nanoparticle nanofluidic scattering spectroscopy (NSS).*** *a) Front view of the nanofluidic chip mounted in the aluminium holder of the chuck, showing the chip surface that faces the microscope objective. The Peltier elements can be seen on the four sides of the aluminium frame. b) Rear view of the assembled chuck showing the flow plate and metal cannulas. The metal cannulas can be filled with liquids by a syringe and connected to gas tubes via Luer-Lock couplings, enabling liquid loading and nitrogen pressure control. c) Schematic illustration of selective pressure-driven liquid exchange. The inlets are filled with either CTAB solution (yellow), or water (blue) or left empty (grey). By applying N_2 overpressure to designated inlets, the composition inside the nanochannels containing the single Au nanoparticles can be rapidly switched between water and CTAB solution.*

Figure **6-4a** shows an overview of the central nanofluidic region, where arrays of parallel nanochannels containing lithographically fabricated Au nanoparticles are connected to opposing microchannels. Higher-magnification dark-field imaging at 50X (**Figure 6-4c**) allows visualization of individual nanochannels and localization of single Au nanoparticles (160 nm × 40 nm × 20 nm) confined within nanochannels with a cross-sectional area of 200 × 200 nm^2. After spatial alignment of a nm nanochannel containing a single Au nanoparticle within the spectrometer slit, scattering spectra were acquired at 1 frame per second rate from several specific regions along the nanochannel (**Figure 6-4d**): (i) the nanoparticle-containing region (NP-3), (ii) two nanoparticle-free sections located closer to the water and CTAB microchannels, respectively, and (iii) two independent reference nanochannels (Ref-1 and Ref-5) continuously filled with MilliQ water. Spectra were recorded using the CCD "multitrack" acquisition mode to improve signal-to-noise while maintaining spectral resolution. In this mode, seven adjacent pixel rows along the slit height were vertically binned, corresponding to a spatial sampling length of approximately 4.2 μm along the nanochannel, while no binning was applied in the wavelength direction to preserve spectral resolution required for centroid determination. Representative spectra recorded with water in the nanochannels are shown in Figure **6-4e**. The nanoparticle-containing region exhibits a pronounced LSPR maximum near 685 nm. Spectra obtained from empty nanochannel regions display a broad spectral maximum arising from the combined wavelength-dependent response of the illumination source, optical components, spectrometer grating, detector sensitivity, and scattering from the nanochannel itself, rather than from a plasmonic resonance[61,155].

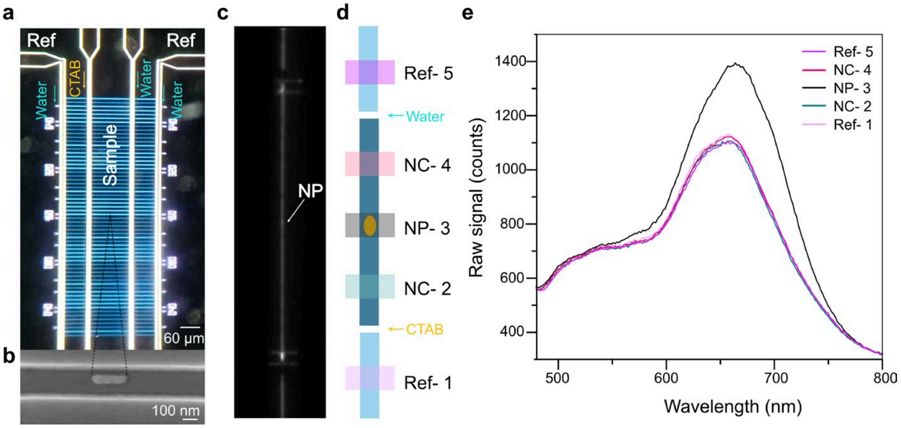

Figure 6-4. ***Layout of the fluidic systems on the chip and definition of nanochannel sections used for nanofluidic scattering spectroscopy of CTAB adsorption on a single Au nanoparticle.*** *a) The dark field microscopy image of the nanofluidic region of the center of the fluidic system, as seen with 10X magnification. What is seen is the array of sample nanochannels with single Au nanoparticles inside, in the center of the image. They are connected to the in- and outlet microfluidic system to the left and right respectively running across the image from top to bottom. One microchannel is filled with 70 mM CTAB solution while the opposing microchannel with water. Also visible are the two reference fluidic systems always filled with water and located to the left and right of the sample fluidic system, respectively. b) The representative SEM image obtained of a rod-shaped Au nanoparticle that is 160 nm long, 40 nm wide and 20 nm high in a 200 nm square cross-section nanochannel, as used for the CTAB adsorption experiment. c) Dark field scattering image taken at 50X magnification of a single nanofluidic channel of the same dimensions as specified in (b). The sample nanochannel has a length of 120 µm. At the lower and upper end of the sample nanochannel, the two reference nanochannels are also visible. Finally, while the microchannels are not visible due to the angle of illumination used in the measurement being parallel to them, the faint horizontal lines correspond to the edges of the microchannels connected to the sample nanochannel. The lower microchannel transports 70 mM CTAB solution and the upper microchannel transports MilliQ water. d) Schematic representing the different sections along the nanochannel from which scattering spectra are collected during the experiment. Each section*

corresponds to 7 binned pixels, corresponding to a length of ca. 4.2 µm. e) The obtained scattering spectra for each of the five sections studied. Notably, the spectrum recorded from the nanoparticle-containing region is the brightest and exhibits a maximum at ca. 685 nm, which is red-shifted compared to the spectra obtained from the empty nanochannel sections and originates from the LSPR of the Au nanoparticle. The empty nanochannel sections also exhibit a broad spectral maximum. This feature does not arise from a plasmonic resonance but instead reflects the combined wavelength-dependent response of the experimental setup, including the spectral intensity distribution of the LED illumination source, the transmission characteristics of the optical components, the diffraction efficiency of the spectrometer grating, and the quantum efficiency of the CCD detector[60,90,156]*. In addition, the nanochannels themselves scatter light efficiently due to the refractive index contrast between the* SiO_2 *channel walls and the liquid interior, resulting in a structured broadband scattering background onto which the nanoparticle LSPR contribution is superimposed.*

After optical alignment of a nanochannel containing a single Au nanoparticle within the spectrometer slit, adsorption measurements were performed under controlled liquid exchange conditions using the microfluidic inlet system of the nanofluidic chip holder. The Au nanoparticle was sequentially exposed to MilliQ water for 15 min, followed by 70 mM CTAB solution for 30 min and a subsequent 15 min water rinse. This water–CTAB–water sequence was repeated twice to investigate adsorption and desorption behaviour under repeated liquid exchange. Spectra obtained from the reference region Ref-5 were subtracted frame-by-frame from spectra recorded at the nanoparticle position NP-3 to compensate for illumination fluctuations and instrumental drift. Referenced scattering spectra obtained during the first exposure cycle are shown in **Figure 6-5a**. Introduction of CTAB into the nanochannel results in a modification of the nanoparticle scattering spectrum, reflecting changes in the local dielectric environment associated with surfactant adsorption at the nanoparticle surface. The temporal evolution of this response was quantified by extracting the LSPR centroid position using the centroid analysis procedure developed by Dahlin and al.[127], yielding the time-dependent $\Delta\lambda_{LSPR}$ as shown in **Figure 6-5b**.

Evidently, $\Delta\lambda_{LSPR}$ exhibits a spectral-red shift upon introduction of CTAB, indicating the adsorption of surfactant molecules onto the Au nanoparticle surface on a time scale of 5 min, similar to what we have seen in the Pt nanoparticle ensemble experiments (**Chapter 5**). The temporal response of $\Delta\lambda_{LSPR}$, upon liquid exchange indicates that CTAB molecules rapidly reach the nanoparticle surface, suggesting that adsorption kinetics are unlikely to be limited by mass transport. Upon a subsequent rinse with MilliQ water, $\Delta\lambda_{LSPR}$ remains almost unchanged, indicating only minimal desorption of loosely bound CTAB molecules. Accordingly, also a second CTAB adsorption step only induces minimal change to $\Delta\lambda_{LSPR}$ (**Figure 6-5b**). Interestingly, upon a second rinsing step, we observe a larger blue shift of $\Delta\lambda_{LSPR}$, which indicates more pronounced CTAB desorption compared to the first rinse, which subsequently also is recovered when again exposing the Au particle to the CTAB solution.

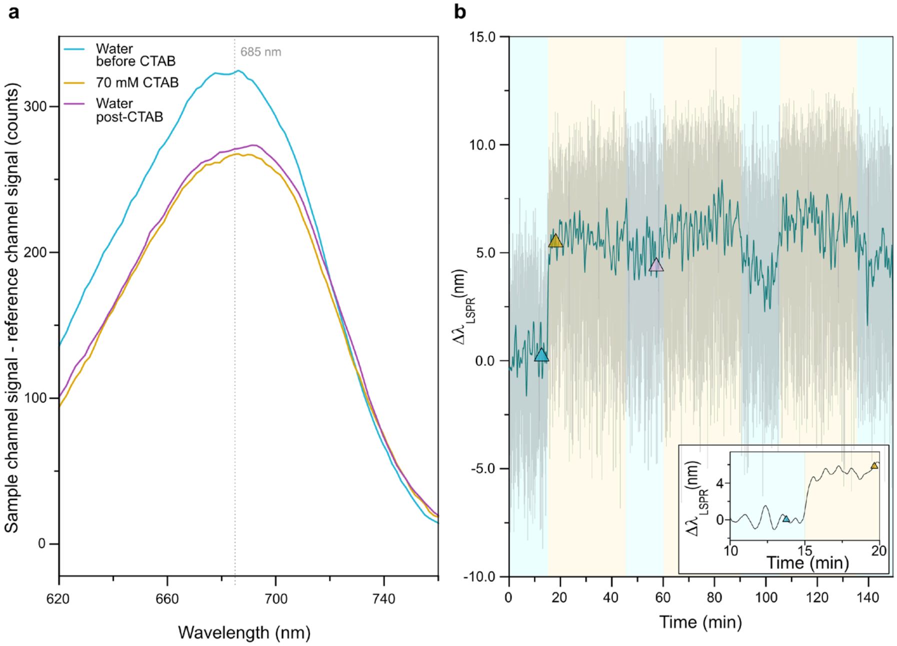

Figure 6-5. ***Representative CTAB adsorption experiment on a single Au nanoparticle localized inside a nanofluidic channel.*** *a) Referenced dark-field scattering spectra extracted from the nanoparticle position (region NP-3 in* ***Figure 6-4d****) at representative stages of the first CTAB exposure cycle, including prior to surfactant introduction (MilliQ water), early adsorption, intermediate adsorption, steady-state exposure to 70 mM CTAB solution, and subsequent rinsing with water. Spectra were obtained after subtraction of the simultaneously recorded reference nanochannel spectrum to correct for illumination fluctuations. The vertical dashed line indicates the approximate LSPR peak position (~685 nm). b) Temporal evolution of $\Delta\lambda_{LSPR}$ extracted from referenced spectra using the centroid fitting procedure*[127] *(grey trace), and filtered with a median despiking and a Savitzky-Golay smoothing (green trace). Blue shaded regions denote MilliQ water in the nanochannel and yellow shaded regions denote exposure to 70 mM CTAB solution. The (Δ) symbols indicate the time points at which the corresponding spectra shown in (a) were acquired. The inset highlights the first 5 min of the initial CTAB exposure cycle, illustrating the stable $\Delta\lambda_{LSPR}$ in water prior to liquid exchange, the rapid red shift immediately following CTAB introduction, and the subsequent gradual transition toward a new steady-state value. This*

behaviour indicates rapid delivery of CTAB to the nanoparticle surface under nanofluidic confinement, followed by slower adsorption and/or interfacial restructuring processes that govern the overall response timescale. Spectra were acquired at 1 fps.

The proof-of-principle result I have presented here has several important implications looking forward. The first one is that it demonstrates that CTAB adsorption kinetics measurements on single nanoparticles localized inside a nanofluidic channel indeed are possible using the dark-field scattering signal of the system as the readout. Furthermore, the initial measurement on an Au nanoparticle revealed adsorption kinetics that qualitatively were similar to the results obtained for the ensemble of Pt nanoparticles in terms of timescales and absolute $\Delta\lambda_{LSPR}$, reached. Quantitatively, there are also clear differences, such as the exact time scale or what was observed upon rinsing. The second implication from this proof-of-principle is that it appears possible to extend the experimental sequence with a catalysis step also in the nanofluidic setting, and to use the NSS readout from sample positions NC-2 and NC-4 (**Figure 6-4d**) to assess the catalytic turnover in analogy to Altenburger et al[61]. This approach potentially creates a closed reaction environment surrounding the nanoparticle, enabling well-defined initial conditions and time-resolved monitoring of catalytic reactions analogous to the catalytic protocol established for nanoparticle ensembles in **Chapter 5**. Therefore, building upon this proof of concept, my future work will focus on implementing such single particle experiments to investigate how different surfactant aggregates, formed under controlled adsorption conditions, influence catalytic reactivity at the level of a single nanoparticle[157]. Such studies would directly bridge ensemble and single nanoparticle investigations, thereby enabling direct correlation between ligand adsorption structure, interfacial dynamics, and catalytic performance at the level of an individual nanoparticle.

7 Conclusions and Outlook

This thesis establishes nanoplasmonic sensing as a quantitative approach for probing ligand adsorption and its impact on catalytic oxidation reaction of ascorbic acid on metallic nanoparticles under controlled fluidic conditions. By combining ensemble measurements on lithographically fabricated Pt nanoparticle arrays with single-particle nanofluidic scattering spectroscopy (NSS), a consistent experimental framework was developed to investigate surfactant–nanoparticle interactions across ensemble and single-particle investigations.

At the ensemble level, localized surface plasmon resonance (LSPR) centroid tracking enabled quantitative monitoring of CTAB adsorption and desorption dynamics. Controlled water–CTAB–water exchange cycles revealed partially irreversible binding under the investigated conditions. A $NaBH_4$-based cleaning protocol was shown to effectively remove surface-bound surfactants without degrading catalytic performance, and ToF-SIMS analysis confirmed the removal of bromide-containing species. Systematic variations in CTAB solution concentrations demonstrated varying surfactant surface coverage which directly impacted the catalytic oxidation of ascorbic acid, establishing a direct link between optical centroid shifts and changes in catalytic rate and selectivity.

The methodology was subsequently extended to single-particle measurements using Nanofluidic Scattering Microscopy/Spectroscopy (NSM/NSS). A nanofluidic chip holder enabling pressure-driven liquid exchange allowed implementation of the same water–CTAB–water protocol at the level of an individual Au nanoparticle. Time-resolved centroid tracking revealed adsorption-induced red shifts comparable in magnitude to those observed in ensemble measurements, indicating consistent dielectric responses across ensemble and single-particle configurations. Repeated liquid-exchange cycles showed incomplete recovery of the LSPR position upon rinsing and reproducible changes of the optical response. These observations demonstrate that single-nanoparticle plasmonic measurements provide access to adsorption behaviour at the level of an individual nanoparticle, complementing ensemble nanoparticles' measurements.

Taken together, the results demonstrate that centroid-based nanoplasmonic sensing provides a robust and transferable metric for quantifying ligand adsorption in both ensemble and single-particle configurations. The use of identical liquid-exchange protocols across platforms establishes a direct methodological bridge between averaged catalytic behaviour and the response of individual nanoparticles.

Looking forward, implementing catalytic reactions within nanofluidic confinement using a batch-reactor concept would enable direct correlation between ligand coverage and catalytic turnover at the single-particle level. Such experiments would provide insight into particle-to-particle variability in catalytic response and clarify how interfacial modification influences catalytic performance. Extending the approach to different surfactant architectures and aggregate states would further advance understanding of how molecular organization at the nanoparticle interface affects both optical response and catalytic behaviour. Ultimately, the integration of nanoplasmonic sensing with controlled nanofluidic environments offers a promising pathway toward mechanistic studies of dynamic ligand–catalyst interfaces under well-defined conditions.

Acknowledgments

I thank Professor Christoph Langhammer for the opportunity to carry out my doctoral research in his group, establishing the research framework and for feedback.

I am especially grateful to my co-supervisors. Dr. Joachim Fritzsche has been an invaluable source of practical nanofabrication solutions and creative problem-solving. I thank Dr. Björn Altenburger for support with experiments and data analysis, as well as for many constructive discussions. I also thank Dr. Sara Nilsson for her help at the beginning of my PhD, especially when I started working with the XNano system.

I also thank Professor Henrik Grönbeck for answering my questions and for numerous appreciated discussions.

Lova, Carl, and Bohdan, thank you for your help, encouragement, and for making daily work more enjoyable.

Finally, I thank my family and friends for their encouragement and patience throughout this journey. Their support has been a steady source of strength. I extend my gratitude to everyone in chemical physics for their help and insights in developing this thesis.

I also acknowledge the European Research Council (ERC) for funding the project, and the Chalmers MC2 cleanroom facility, where parts of this work were carried out.

References

1. Feynman, R. There's plenty of room at the bottom. *Engineering and Science* **23**, 22–36 (1960).
2. Hughes, K. J. *et al.* Nanoscience in Action: Unveiling Emerging Trends in Materials and Applications. *ACS Omega* **10**, 7530–7548 (2025).
3. Mekuye, B. & Abera, B. Nanomaterials: An overview of synthesis, classification, characterization, and applications. *Nano Select* **4**, 486–501 (2023).
4. Abid, N. *et al.* Synthesis of nanomaterials using various top-down and bottom-up approaches, influencing factors, advantages, and disadvantages: A review. *Advances in Colloid and Interface Science* **300**, 102597 (2022).
5. Muthukrishnan, S., Bhakya, S. & Ramalingam, V. Metal nanoparticles synthesis: an overview of different synthesis methods, mode of action and their biomedical application. *Discov Appl Sci* **7**, 1079 (2025).
6. Thanh, N. T. K., Maclean, N. & Mahiddine, S. Mechanisms of Nucleation and Growth of Nanoparticles in Solution. *Chem. Rev.* **114**, 7610–7630 (2014).
7. Bhattacharjee, K. & Prasad, B. L. V. Surface functionalization of inorganic nanoparticles with ligands: a necessary step for their utility. *Chem. Soc. Rev.* **52**, 2573–2595 (2023).

8. Fritz, G., Schädler, V., Willenbacher, N. & Wagner, N. J. Electrosteric Stabilization of Colloidal Dispersions. *Langmuir* **18**, 6381–6390 (2002).
9. Safo, I. A., Werheid, M., Dosche, C. & Oezaslan, M. The role of polyvinylpyrrolidone (PVP) as a capping and structure-directing agent in the formation of Pt nanocubes. *Nanoscale Adv.* **1**, 3095–3106 (2019).
10. Heuer-Jungemann, A. *et al.* The Role of Ligands in the Chemical Synthesis and Applications of Inorganic Nanoparticles. *Chem. Rev.* **119**, 4819–4880 (2019).
11. Huang, L. *et al.* Shape-Control of Pt–Ru Nanocrystals: Tuning Surface Structure for Enhanced Electrocatalytic Methanol Oxidation. *J. Am. Chem. Soc.* **140**, 1142–1147 (2018).
12. Lewis, L. N. Chemical catalysis by colloids and clusters. *Chem. Rev.* **93**, 2693–2730 (1993).
13. An, K., Alayoglu, S., Ewers, T. & Somorjai, G. A. Colloid chemistry of nanocatalysts: A molecular view. *Journal of Colloid and Interface Science* **373**, 1–13 (2012).
14. Narayanan, R. & El-Sayed, M. A. Shape-Dependent Catalytic Activity of Platinum Nanoparticles in Colloidal Solution. *Nano Lett.* **4**, 1343–1348 (2004).

15. Narayanan, R. & El-Sayed, M. A. Catalysis with Transition Metal Nanoparticles in Colloidal Solution: Nanoparticle Shape Dependence and Stability. *J. Phys. Chem. B* **109**, 12663–12676 (2005).
16. Eyring, H. The Activated Complex in Chemical Reactions. *The Journal of Chemical Physics* **3**, 107–115 (1935).
17. Ka, B. Catalysts of Life: Unveiling the Mysteries of Enzymes. *Journal of Medicine and Medical Sciences* 1–2 (2024).
18. McGovern, P. *et al.* Early Neolithic wine of Georgia in the South Caucasus. *Proc. Natl. Acad. Sci. U.S.A.* **114**, (2017).
19. Liu, L. *et al.* Fermented beverage and food storage in 13,000 y-old stone mortars at Raqefet Cave, Israel: Investigating Natufian ritual feasting. *Journal of Archaeological Science: Reports* **21**, 783–793 (2018).
20. W., W. The Manufacture of Sulphuric Acid (Contact Process). *Nature* **116**, 385–386 (1925).
21. Mperiju, T. *et al.* Optimized Production of High Purity Sulphuric Acid via Contact Process. *LOMR* **2**, 1–13 (2023).
22. The Haber Process. *Nature* **111**, 101–102 (1923).
23. List, B., Lerner, R. A. & Barbas, C. F. Proline-Catalyzed Direct Asymmetric Aldol Reactions. *J. Am. Chem. Soc.* **122**, 2395–2396 (2000).

24. Ertl, G. Reactions at Surfaces: From Atoms to Complexity (Nobel Lecture). *Angew Chem Int Ed* **47**, 3524–3535 (2008).
25. Samorjai, G. Introduction to Surface Chemistry and Catalysis, 2nd Edition. (2010).
26. Liu, L. & Corma, A. Metal Catalysts for Heterogeneous Catalysis: From Single Atoms to Nanoclusters and Nanoparticles. *Chem. Rev.* **118**, 4981–5079 (2018).
27. Twigg, M. V. Controlling automotive exhaust emissions: successes and underlying science. *Phil. Trans. R. Soc. A.* **363**, 1013–1033 (2005).
28. Hanrieder, E. K., Jentys, A. & Lercher, J. A. Atomistic Engineering of Catalyst Precursors: Dynamic Reordering of PdAu Nanoparticles during Vinyl Acetate Synthesis Enhanced by Potassium Acetate. *ACS Catal.* **5**, 5776–5786 (2015).
29. Pelton, M. & Bryant, G. W. *Introduction to Metal-Nanoparticle Plasmonics*. (2013).
30. Langhammer, C., Yuan, Z., Zorić, I. & Kasemo, B. Plasmonic Properties of Supported Pt and Pd Nanostructures. *Nano Lett.* **6**, 833–838 (2006).
31. Hu, M. *et al.* Dark-field microscopy studies of single metal nanoparticles: understanding the factors that influence the linewidth of the localized surface plasmon resonance. *J. Mater. Chem.* **18**, 1949 (2008).

32. Nehl, C. L. *et al.* Scattering Spectra of Single Gold Nanoshells. *Nano Lett.* **4**, 2355–2359 (2004).
33. Petryayeva, E. & Krull, U. J. Localized surface plasmon resonance: Nanostructures, bioassays and biosensing—A review. *Analytica Chimica Acta* **706**, 8–24 (2011).
34. Špačková, B., Šípová-Jungová, H., Käll, M., Fritzsche, J. & Langhammer, C. Nanoplasmonic–Nanofluidic Single-Molecule Biosensors for Ultrasmall Sample Volumes. *ACS Sens.* **6**, 73–82 (2021).
35. Anker, J., Hall, W. & Lyandres, O. Biosensing with plasmonic nanosensors. *Nature Mater* **7**, 442–453 (2008).
36. Martvall, V. *et al.* Accelerating Plasmonic Hydrogen Sensors for Inert Gas Environments by Transformer-Based Deep Learning. *ACS Sens.* **10**, 376–386 (2025).
37. Theodoridis, A., Andersson, C., Nilsson, S., Fritzsche, J. & Langhammer, C. A Catalytic-Plasmonic Pt Nanoparticle Sensor for Hydrogen Detection in High-Humidity Environments. *ACS Sens.* **10**, 8983–8994 (2025).
38. Tanyeli, I. *et al.* Nanoplasmonic NO_2 Sensor with a Sub-10 Parts per Billion Limit of Detection in Urban Air. *ACS Sens.* **7**, 1008–1018 (2022).

39. Lerch, S. *et al.* Robust Colloidal Synthesis of Palladium–Gold Alloy Nanoparticles for Hydrogen Sensing. *ACS Appl. Mater. Interfaces* **13**, 45758–45767 (2021).

40. Darmadi, I., Khairunnisa, S. Z., Tomeček, D. & Langhammer, C. Optimization of the Composition of PdAuCu Ternary Alloy Nanoparticles for Plasmonic Hydrogen Sensing. *ACS Appl. Nano Mater.* **4**, 8716–8722 (2021).

41. Alekseeva, S., Nedrygailov, I. I. & Langhammer, C. Single Particle Plasmonics for Materials Science and Single Particle Catalysis. *ACS Photonics* **6**, 1319–1330 (2019).

42. Lu, L., Zou, S. & Fang, B. The Critical Impacts of Ligands on Heterogeneous Nanocatalysis: A Review. *ACS Catal.* **11**, 6020–6058 (2021).

43. Kwan Li, K., Wu, C.-Y., Yang, T.-H., Qin, D. & Xia, Y. Quantification, Exchange, and Removal of Surface Ligands on Noble-Metal Nanocrystals. *Acc. Chem. Res.* **56**, 1517–1527 (2023).

44. Sadeghmoghaddam, E., Lam, C., Choi, D. & Shon, Y.-S. Synthesis and catalytic properties of alkanethiolate-capped Pd nanoparticles generated from sodium S-dodecylthiosulfate. *J. Mater. Chem.* **21**, 307–312 (2011).

45. Vargas, K. M., San, K. A. & Shon, Y.-S. Isolated Effects of Surface Ligand Density on the Catalytic Activity and Selectivity of Palladium Nanoparticles. *ACS Appl. Nano Mater.* **2**, 7188–7196 (2019).
46. Sadeghmoghaddam, E., Gu, H. & Shon, Y.-S. Pd Nanoparticle-Catalyzed Isomerization vs Hydrogenation of Allyl Alcohol: Solvent-Dependent Regioselectivity. *ACS Catal.* **2**, 1838–1845 (2012).
47. Gavia, D. J. & Shon, Y.-S. Controlling Surface Ligand Density and Core Size of Alkanethiolate-Capped Pd Nanoparticles and Their Effects on Catalysis. *Langmuir* **28**, 14502–14508 (2012).
48. Gavia, D. J., Maung, M. S. & Shon, Y.-S. Water-Soluble Pd Nanoparticles Synthesized from ω-Carboxyl- *S* -Alkanethiosulfate Ligand Precursors as Unimolecular Micelle Catalysts. *ACS Appl. Mater. Interfaces* **5**, 12432–12440 (2013).
49. Da Silva, F. P., Fiorio, J. L. & Rossi, L. M. Tuning the Catalytic Activity and Selectivity of Pd Nanoparticles Using Ligand-Modified Supports and Surfaces. *ACS Omega* **2**, 6014–6022 (2017).
50. Kwon, S. G. *et al.* Capping Ligands as Selectivity Switchers in Hydrogenation Reactions. *Nano Lett.* **12**, 5382–5388 (2012).
51. Pankhurst, J. R., Guntern, Y. T., Mensi, M. & Buonsanti, R. Molecular tunability of surface-functionalized metal nanocrystals for selective electrochemical CO_2 reduction. *Chem. Sci.* **10**, 10356–10365 (2019).

52. Jancke, S. & Rossner, C. Functionalization with polymer ligands enhances the catalytic activity of surfactant-stabilized gold nanoparticles. *Nanoscale* **17**, 14271–14277 (2025).
53. Fresch, B. & Remacle, F. Tuning the Properties of Pd Nanoclusters by Ligand Coatings: Electronic Structure Computations on Phosphine, Thiol, and Mixed Phosphine–Thiol Ligand Shells. *J. Phys. Chem. C* **118**, 9790–9800 (2014).
54. Chen, L., Moura, P., Medlin, J. W. & Grönbeck, H. Multiple Roles of Alkanethiolate-Ligands in Direct Formation of H_2 O_2 over Pd Nanoparticles. *Angew Chem Int Ed* **61**, e202213113 (2022).
55. Xu, W., Kong, J. S., Yeh, Y.-T. E. & Chen, P. Single-molecule nanocatalysis reveals heterogeneous reaction pathways and catalytic dynamics. *Nature Mater* **7**, 992–996 (2008).
56. Xu, W., Kong, J. S. & Chen, P. Probing the catalytic activity and heterogeneity of Au-nanoparticles at the single-molecule level. *Phys. Chem. Chem. Phys.* **11**, 2767 (2009).
57. Han, K. S., Liu, G., Zhou, X., Medina, R. E. & Chen, P. How Does a Single Pt Nanocatalyst Behave in Two Different Reactions? A Single-Molecule Study. *Nano Lett.* **12**, 1253–1259 (2012).

58. Gao, W., Hood, Z. D. & Chi, M. Interfaces in Heterogeneous Catalysts: Advancing Mechanistic Understanding through Atomic-Scale Measurements. *Acc. Chem. Res.* **50**, 787–795 (2017).

59. Levin, S. *et al.* A nanofluidic device for parallel single nanoparticle catalysis in solution. *Nat Commun* **10**, 4426 (2019).

60. Altenburger, B. *et al.* Label-Free Imaging of Catalytic H_2 O_2 Decomposition on Single Colloidal Pt Nanoparticles Using Nanofluidic Scattering Microscopy. *ACS Nano* **17**, 21030–21043 (2023).

61. Altenburger, B., Fritzsche, J. & Langhammer, C. Femtoliter Batch Reactors for Nanofluidic Scattering Spectroscopy Analysis of Catalytic Reactions on Single Nanoparticles. *Small Methods* 2500693 (2025).

62. The History/Development of Single Particle Nanocatalysis. in *Single Particle Nanocatalysis* 1–8 (2019).

63. Giorgio, S. *et al.* Environmental electron microscopy (ETEM) for catalysts with a closed E-cell with carbon windows. *Ultramicroscopy* **106**, 503–507 (2006).

64. He, B., Zhang, Y., Liu, X. & Chen, L. In-situ Transmission Electron Microscope Techniques for Heterogeneous Catalysis. *ChemCatChem* **12**, 1853–1872 (2020).

65. Williamson, M. J., Tromp, R. M., Vereecken, P. M., Hull, R. & Ross, F. M. Dynamic microscopy of nanoscale cluster growth at the solid–liquid interface. *Nature Mater* **2**, 532–536 (2003).

66. De Jonge, N., Bigelow, W. C. & Veith, G. M. Atmospheric Pressure Scanning Transmission Electron Microscopy. *Nano Lett.* **10**, 1028–1031 (2010).

67. Pu, S., Gong, C. & Robertson, A. W. Liquid cell transmission electron microscopy and its applications. *R. Soc. open sci.* **7**, 191204 (2020).

68. Xu, L. *et al.* Filming evolution dynamics of Hg nanodroplets mediated at solid-gas and solid-liquid interfaces by in-situ TEM. *Nat Commun* **16**, 3684 (2025).

69. Buckett, M. I. *et al.* Electron irradiation damage in oxides. *Ultramicroscopy* **29**, 217–227 (1989).

70. Jiang, N. Electron irradiation effects in transmission electron microscopy: Random displacements and collective migrations. *Micron* **171**, 103482 (2023).

71. Kuwauchi, Y., Yoshida, H., Akita, T., Haruta, M. & Takeda, S. Intrinsic Catalytic Structure of Gold Nanoparticles Supported on TiO_2. *Angew Chem Int Ed* **51**, 7729–7733 (2012).

72. Meirer, F. & Weckhuysen, B. M. Spatial and temporal exploration of heterogeneous catalysts with synchrotron radiation. *Nat Rev Mater* **3**, 324–340 (2018).

73. Ebejer, N. *et al.* Scanning Electrochemical Cell Microscopy: A Versatile Technique for Nanoscale Electrochemistry and Functional Imaging.

74. Chen, P. *et al.* Single-molecule fluorescence imaging of nanocatalytic processes. *Chem. Soc. Rev.* **39**, 4560 (2010).

75. Chen, P., Xu, W., Zhou, X., Panda, D. & Kalininskiy, A. Single-nanoparticle catalysis at single-turnover resolution. *Chemical Physics Letters* **470**, 151–157 (2009).

76. Mao, X., Liu, C., Hesari, M., Zou, N. & Chen, P. Super-resolution imaging of non-fluorescent reactions via competition. *Nat. Chem.* **11**, 687–694 (2019).

77. Van Schrojenstein Lantman, E. M., Deckert-Gaudig, T., Mank, A. J. G., Deckert, V. & Weckhuysen, B. M. Catalytic processes monitored at the nanoscale with tip-enhanced Raman spectroscopy. *Nature Nanotech* **7**, 583–586 (2012).

78. Hartman, T., Wondergem, C. S., Kumar, N., Van Den Berg, A. & Weckhuysen, B. M. Surface- and Tip-Enhanced Raman Spectroscopy in Catalysis. *J. Phys. Chem. Lett.* **7**, 1570–1584 (2016).

79. Kumar, N., Wondergem, C. S., Wain, A. J. & Weckhuysen, B. M. In Situ Nanoscale Investigation of Catalytic Reactions in the Liquid Phase Using Zirconia-Protected Tip-Enhanced Raman Spectroscopy Probes. *J. Phys. Chem. Lett.* **10**, 1669–1675 (2019).

80. Li, J. F. *et al.* Shell-isolated nanoparticle-enhanced Raman spectroscopy. *Nature* **464**, 392–395 (2010).

81. Hartman, T., Geitenbeek, R. G., Whiting, G. T. & Weckhuysen, B. M. Operando monitoring of temperature and active species at the single catalyst particle level. *Nat Catal* **2**, 986–996 (2019).

82. Stolaś, A., Darmadi, I., Nugroho, F. A. A., Moth-Poulsen, K. & Langhammer, C. Impact of Surfactants and Stabilizers on Palladium Nanoparticle–Hydrogen Interaction Kinetics: Implications for Hydrogen Sensors. *ACS Appl. Nano Mater.* **3**, 2647–2653 (2020).

83. Larsson, E. M., Alegret, J., Käll, M. & Sutherland, D. S. Sensing Characteristics of NIR Localized Surface Plasmon Resonances in Gold Nanorings for Application as Ultrasensitive Biosensors. *Nano Lett.* **7**, 1256–1263 (2007).

84. Liu, S. *et al. In Situ* Plasmonic Nanospectroscopy of the CO Oxidation Reaction over Single Pt Nanoparticles. *ACS Nano* **13**, 6090–6100 (2019).

85. Albinsson, D. *et al.* Copper catalysis at operando conditions—bridging the gap between single nanoparticle probing and catalyst-bed-averaging. *Nat Commun* **11**, 4832 (2020).
86. Albinsson, D. *et al.* Shedding Light on CO Oxidation Surface Chemistry on Single Pt Catalyst Nanoparticles Inside a Nanofluidic Model Pore. *ACS Catal.* **11**, 2021–2033 (2021).
87. Nilsson, S. *et al.* The Role of Grain Boundary Sites for the Oxidation of Copper Catalysts during the CO Oxidation Reaction. *ACS Nano* **17**, 20284–20298 (2023).
88. Klein Moberg, H. *et al.* Deep-learning-enabled online mass spectrometry of the reaction product of a single catalyst nanoparticle. *Nat Commun* **16**, 7203 (2025).
89. Levin, S. *et al.* Nanofluidic Trapping of Faceted Colloidal Nanocrystals for Parallel Single-Particle Catalysis. *ACS Nano* **16**, 15206–15214 (2022).
90. Altenburger, B., Fritzsche, J. & Langhammer, C. Visible Light Spectroscopy of Liquid Solutes from Femto- to Attoliter Volumes Inside a Single Nanofluidic Channel. *ACS Nano* **19**, 2857–2869 (2025).
91. Maier, S. A. *Plasmonics: Fundamentals and Applications*. (Springer, New York, 2007).

92. Hartland, G. V., Besteiro, L. V., Johns, P. & Govorov, A. O. What's so Hot about Electrons in Metal Nanoparticles? *ACS Energy Lett.* **2**, 1641–1653 (2017).
93. Willets, K. A. & Van Duyne, R. P. Localized Surface Plasmon Resonance Spectroscopy and Sensing. *Annu. Rev. Phys. Chem.* **58**, 267–297 (2007).
94. Mayer, K. M. & Hafner, J. H. Localized Surface Plasmon Resonance Sensors. *Chem. Rev.* **111**, 3828–3857 (2011).
95. Langhammer, C. & Larsson, E. M. Nanoplasmonic In Situ Spectroscopy for Catalysis Applications. *ACS Catal.* **2**, 2036–2045 (2012).
96. Novo, C., Funston, A. M. & Mulvaney, P. Direct observation of chemical reactions on single gold nanocrystals using surface plasmon spectroscopy. *Nature Nanotech* **3**, 598–602 (2008).
97. Taylor, A. B. & Zijlstra, P. Single-Molecule Plasmon Sensing: Current Status and Future Prospects. *ACS Sens.* **2**, 1103–1122 (2017).
98. McCoy, D. E., Shneidman, A. V., Davis, A. L. & Aizenberg, J. Finite-difference Time-domain (FDTD) Optical Simulations: A Primer for the Life Sciences and Bio-Inspired Engineering. *Micron* **151**, 103160 (2021).
99. Fredriksson, H. *et al.* Hole–Mask Colloidal Lithography. *Advanced Materials* **19**, 4297–4302 (2007).

100. Olson, J. *et al.* Optical characterization of single plasmonic nanoparticles. *Chem. Soc. Rev.* **44**, 40–57 (2015).

101. Fan, X., Zheng, W. & Singh, D. J. Light scattering and surface plasmons on small spherical particles. *Light Sci Appl* **3**, e179–e179 (2014).

102. Hayashi, H. & Hiraoka, N. Accurate Measurements of Dielectric and Optical Functions of Liquid Water and Liquid Benzene in the VUV Region (1–100 eV) Using Small-Angle Inelastic X-ray Scattering. *J. Phys. Chem. B* **119**, 5609–5623 (2015).

103. Johnson, P. B. & Christy, R. W. Optical Constants of the Noble Metals. *Phys. Rev. B* **6**, 4370–4379 (1972).

104. Langhammer, C., Zorić, I., Kasemo, B. & Clemens, B. M. Hydrogen Storage in Pd Nanodisks Characterized with a Novel Nanoplasmonic Sensing Scheme. *Nano Lett.* **7**, 3122–3127 (2007).

105. Darmadi, I., Nugroho, F. A. A. & Langhammer, C. High-Performance Nanostructured Palladium-Based Hydrogen Sensors—Current Limitations and Strategies for Their Mitigation. *ACS Sens.* **5**, 3306–3327 (2020).

106. Jeon, H. B., Tsalu, P. V. & Ha, J. W. Shape Effect on the Refractive Index Sensitivity at Localized Surface Plasmon Resonance Inflection Points of Single Gold Nanocubes with Vertices. *Sci Rep* **9**, 13635 (2019).

107. Miller, M. M. & Lazarides, A. A. Sensitivity of Metal Nanoparticle Surface Plasmon Resonance to the Dielectric Environment. *J. Phys. Chem. B* **109**, 21556–21565 (2005).

108. Fogg, E. T., Hixson, A. N. & Thompson, A. R. Densities and Refractive Indexes for Ethylene Glycol-Water Solutions. *Anal. Chem.* **27**, 1609–1611 (1955).

109. Somorjai, G. & Li, Y. *Introduction to Surface Chemistry and Catalysis*. (Wiley, 2010).

110. Widmer-Cooper, A. & Geissler, P. L. Ligand-Mediated Interactions between Nanoscale Surfaces Depend Sensitively and Nonlinearly on Temperature, Facet Dimensions, and Ligand Coverage. *ACS Nano* **10**, 1877–1887 (2016).

111. Guan, H., Harris, C. & Sun, S. Metal–Ligand Interactions and Their Roles in Controlling Nanoparticle Formation and Functions. *Acc. Chem. Res.* **56**, 1591–1601 (2023).

112. Daniel, M.-C. & Astruc, D. Gold Nanoparticles: Assembly, Supramolecular Chemistry, Quantum-Size-Related Properties, and Applications toward Biology, Catalysis, and Nanotechnology. *Chem. Rev.* **104**, 293–346 (2004).

113. Israelachvili, J. N. *Intermolecular and Surface Forces*. (Elsevier, 2011).

114. Paria, S. & Khilar, K. C. A review on experimental studies of surfactant adsorption at the hydrophilic solid–water interface. *Advances in Colloid and Interface Science* **110**, 75–95 (2004).

115. Kronberg, B., Holmberg, K. & Lindman, B. *Surface Chemistry of Surfactants and Polymers*. (Wiley, 2014).

116. Xia, Y., Xiong, Y., Lim, B. & Skrabalak, S. E. Shape-Controlled Synthesis of Metal Nanocrystals: Simple Chemistry Meets Complex Physics? *Angew Chem Int Ed* **48**, 60–103 (2009).

117. Rossi, L. M., Fiorio, J. L., Garcia, M. A. S. & Ferraz, C. P. Role and fate of capping ligands in colloidally prepared metal nanoparticle catalysts. *Dalton Trans.* **47**, 5889–5915 (2018).

118. Rosen, M. J. *Surfactants and Interfacial Phenomena*. (John Wiley & Sons, Incorporated, 2012).

119. Chenyakin, Y. & Chen, D. D. Y. Determination of Critical Micelle Concentration of Ionic and Non-Ionic Surfactants by Streaming Potential Measurements. *Electrophoresis* **46**, 990–997 (2025).

120. Manojlovic, J. The Krafft temperature of surfactant solutions. *Therm sci* **16**, 631–640 (2012).

121. Striolo, A. & Grady, B. P. Surfactant Assemblies on Selected Nanostructured Surfaces: Evidence, Driving Forces, and Applications. *Langmuir* **33**, 8099–8113 (2017).

122. Mosquera, J., Wang, D., Bals, S. & Liz-Marzán, L. M. Surfactant Layers on Gold Nanorods. *Acc. Chem. Res.* **56**, 1204–1212 (2023).

123. Liu, Z. *et al.* Ligand effect on switching the rate-determining step of water oxidation in atomically precise metal nanoclusters. *Nat Commun* **14**, 3374 (2023).

124. Smith, J. G. & Jain, P. K. The Ligand Shell as an Energy Barrier in Surface Reactions on Transition Metal Nanoparticles. *J. Am. Chem. Soc.* **138**, 6765–6773 (2016).

125. Schulz, F. *et al.* Local Environments Created by the Ligand Coating of Nanoparticles and Their Implications for Sensing and Surface Reactions. *Acc. Chem. Res.* **56**, 2278–2285 (2023).

126. Haes, A. J., Zou, S., Schatz, G. C. & Van Duyne, R. P. Nanoscale Optical Biosensor: Short Range Distance Dependence of the Localized Surface Plasmon Resonance of Noble Metal Nanoparticles. *J. Phys. Chem. B* **108**, 6961–6968 (2004).

127. Dahlin, A. B., Tegenfeldt, J. O. & Höök, F. Improving the Instrumental Resolution of Sensors Based on Localized Surface Plasmon Resonance. *Anal. Chem.* **78**, 4416–4423 (2006).

128. Wen, B., Yang, J., Hu, C., Cai, J. & Zhou, J. Top-Down Fabrication of Ordered Nanophotonic Structures for Biomedical Applications. *Adv Materials Inter* **11**, 2300856 (2024).

129. Levinson, H. J. The challenges and limits to patterning using EUV lithography. in *39th European Mask and Lithography Conference (EMLC 2024)* (eds Behringer, U. F. & Finders, J.) 37 (SPIE, Grenoble, France, 2024). doi:10.1117/12.3029169.

130. Yang, S., Jang, S. G., Choi, D., Kim, S. & Yu, H. K. Nanomachining by Colloidal Lithography. *Small* **2**, 458–475 (2006).

131. Theodoridis, A., Andersson, C., Nilsson, S., Fritzsche, J. & Langhammer, C. A Catalytic-Plasmonic Pt Nanoparticle Sensor for Hydrogen Detection in High-Humidity Environments. *ACS Sens.* **10**, 8983–8994 (2025).

132. Tomeček, D. *et al.* Neural network enabled nanoplasmonic hydrogen sensors with 100 ppm limit of detection in humid air. *Nat Commun* **15**, 1208 (2024).

133. Schulze, G. & Prausnitz, J. M. Solubilities of gases in water at high temperatures. *Ind. Eng. Chem. Fundam.* **20**, 175–177 (1981).

134. Yuan, M. *et al.* A Method for Removing Self-Assembled Monolayers on Gold. *Langmuir* **24**, 8707–8710 (2008).

135. He, J. *et al.* The facile removal of CTAB from the surface of gold nanorods. *Colloids and Surfaces B: Biointerfaces* **163**, 140–145 (2018).

136. Hamon, J. J., Striolo, A. & Grady, B. P. Observing the Effects of Temperature and Surface Roughness on Cetyltrimethylammonium

Bromide Adsorption Using a Quartz-Crystal Microbalance with Dissipation Monitoring. *J Surfact & Detergents* **22**, 1201–1212 (2019).

137. Campbell, C. T. Ultrathin metal films and particles on oxide surfaces: structural, electronic and chemisorptive properties. *Surface Science Reports* **27**, 1–111 (1997).

138. Ansar, S. M. *et al.* Removal of Molecular Adsorbates on Gold Nanoparticles Using Sodium Borohydride in Water. *Nano Lett.* **13**, 1226–1229 (2013).

139. Zhang, X. *et al.* A facile method in removal of PVP ligands from silver nanowires for high performance and reusable SERS substrate. *Spectrochimica Acta Part A: Molecular and Biomolecular Spectroscopy* **228**, 117733 (2020).

140. Li, W., Zhang, M., Zhang, J. & Han, Y. Self-assembly of cetyl trimethylammonium bromide in ethanol-water mixtures. *Front. Chem. China* **1**, 438–442 (2006).

141. Graham, D. J. & Gamble, L. J. Back to the basics of time-of-flight secondary ion mass spectrometry of bio-related samples. I. Instrumentation and data collection. *Biointerphases* **18**, 021201 (2023).

142. Berg, R. W. Investigation of L (+)-Ascorbic acid with Raman spectroscopy in visible and UV light. *Applied Spectroscopy Reviews* **50**, 193–239 (2015).

143. Kékicheff, P., Christenson, H. K. & Ninham, B. W. Adsorption of cetyltrimethylammonium bromide to mica surfaces below the critical micellar concentration. *Colloids and Surfaces* **40**, 31–41 (1989).

144. Carr, A. & Maggini, S. Vitamin C and Immune Function. *Nutrients* **9**, 1211 (2017).

145. Wagner, B. A. & Buettner, G. R. Stability of aqueous solutions of ascorbate for basic research and for intravenous administration. *Advances in Redox Research* **9**, 100077 (2023).

146. Shen, J. *et al.* Ascorbate oxidation by iron, copper and reactive oxygen species: review, model development, and derivation of key rate constants. *Sci Rep* **11**, 7417 (2021).

147. Gómez Ruiz, B., Roux, S., Courtois, F. & Bonazzi, C. Spectrophotometric method for fast quantification of ascorbic acid and dehydroascorbic acid in simple matrix for kinetics measurements. *Food Chemistry* **211**, 583–589 (2016).

148. Berg, R. W. Investigation of L (+)-Ascorbic acid with Raman spectroscopy in visible and UV light. *Applied Spectroscopy Reviews* **50**, 193–239 (2015).

149. Chen, C. *et al.* Platinum nanoparticles inhibit antioxidant effects of vitamin C via ascorbate oxidase-mimetic activity. *J. Mater. Chem. B* **4**, 7895–7901 (2016).

150. Zhou, Y.-T. *et al.* Enzyme-mimetic effects of gold@platinum nanorods on the antioxidant activity of ascorbic acid. *Nanoscale* **5**, 1583 (2013).

151. Špačková, B. *et al.* Label-free nanofluidic scattering microscopy of size and mass of single diffusing molecules and nanoparticles. *Nat Methods* **19**, 751–758 (2022).

152. Iarossi, M., Verma, N. C., Bhattacharya, I. & Meller, A. The Emergence of Nanofluidics for Single-Biomolecule Manipulation and Sensing. *Anal. Chem.* **97**, 8641–8653 (2025).

153. Langhammer, C., Kasemo, B. & Zorić, I. Absorption and scattering of light by Pt, Pd, Ag, and Au nanodisks: Absolute cross sections and branching ratios. *The Journal of Chemical Physics* **126**, 194702 (2007).

154. Altenburger, B., Fritzsche, J. & Langhammer, C. A temperature-controlled chip holder with integrated electrodes for nanofluidic scattering spectroscopy on highly integrated nanofluidic systems. *Microsyst Nanoeng* **12**, 32 (2026).

155. Altenburger, B. Nanofluidic Scattering Microscopy and Spectroscopy for Single Particle Catalysis. Thesis. (2024).

156. Fritzsche, J. *et al.* Single Particle Nanoplasmonic Sensing in Individual Nanofluidic Channels. *Nano Lett.* **16**, 7857–7864 (2016).

157. Atkin, R., Craig, V. S. J., Wanless, E. J. & Biggs, S. Mechanism of cationic surfactant adsorption at the solid–aqueous interface. *Advances in Colloid and Interface Science* **103**, 219–304 (2003).